J. Fluid Mech. (2005), *vol.* 524, *pp.* 143–195.
DOI: 10.1017/S0022112004002514 Printed in the United Kingdom

Studies of interactions of a propagating shock wave with decaying grid turbulence: velocity and vorticity fields

By JUAN H. AGUI[†], GEORGE BRIASSULIS AND YIANNIS ANDREOPOULOS

Experimental Aerodynamics and Fluid Mechanics Laboratory, Department of Mechanical Engineering,
The City College of the City University of New York, New York, NY 10031, USA

(Received 19 September 2003 and in revised form 20 September 2004)

The unsteady interaction of a moving shock wave with nearly homogeneous and isotropic decaying compressible turbulence has been studied experimentally in a large-scale shock tube facility. Rectangular grids of various mesh sizes were used to generate turbulence with Reynolds numbers based on Taylor's microscale ranging from 260 to 1300. The interaction has been investigated by measuring the three-dimensional velocity and vorticity vectors, the full velocity gradient and rate-of-strain tensors with instrumentation of high temporal and spatial resolution. This allowed estimates of dilatation, compressible dissipation and dilatational stretching to be obtained. The time-dependent signals of enstrophy, vortex stretching/tilting vector and dilatational stretching vector were found to exhibit a rather strong intermittent behaviour which is characterized by high-amplitude bursts with values up to 8 times their r.m.s. within periods of less violent and longer lived events. Several of these bursts are evident in all the signals, suggesting the existence of a dynamical flow phenomenon as a common cause. Fluctuations of all velocity gradients in the longitudinal direction are amplified significantly downstream of the interaction. Fluctuations of the velocity gradients in the lateral directions show no change or a minor reduction through the interaction. Root mean square values of the lateral vorticity components indicate a 25% amplification on average, which appears to be very weakly dependent on the shock strength. The transmission of the longitudinal vorticity fluctuations through the shock appears to be less affected by the interaction than the fluctuations of the lateral components. Non-dissipative vortex tubes and irrotational dissipative motions are more intense in the region downstream of the shock. There is also a significant increase in the number of events with intense rotational and dissipative motions. Integral length scales and Taylor's microscales were reduced after the interaction with the shock in all investigated flow cases. The integral length scales in the lateral direction increase at low Mach numbers and decrease during strong interactions. It appears that in the weakest of the present interactions, turbulent eddies are compressed drastically in the longitudinal direction while their extent in the normal direction remains relatively the same. As the shock strength increases the lateral integral length scales increase while the longitudinal ones decrease. At the strongest interaction of the present flow cases turbulent eddies are compressed in both directions. However, even at the highest Mach number the issue is more complicated since amplification of the lateral scales has been observed

---

[†] Present address: NASA Glenn Research Center, Cleveland, OH 44135, USA.

in flows with fine grids. Thus the outcome of the interaction strongly depends on the initial conditions.

---

1. Introduction

Interactions of shock waves with turbulent flows are of great practical importance in external and internal aerodynamics of engineering applications since they considerably modify the fluid field by vorticity and entropy production and transport. Of particular interest is the interaction of shock waves propagating inside a turbulent flow, which can be considered as nearly isotropic and nearly homogeneous. Travelling shock waves or expansion waves can be generated inside turbines or compressors of turbine engines as a result of unsteady flow phenomena. New concepts of engines based on pulse detonations also involve travelling shock waves and related unsteady flow phenomena. These moving waves can interact with rotating or stationary blades as well as with the flow and may result in phenomena which can affect the operation and performance of the engine.

Past work has shown that the interaction between the shock wave and turbulent flow is mutual and the coupling between them is very strong. Complex linear and nonlinear mechanisms are involved which can cause considerable changes in the structure of turbulence and its statistical properties and alter the dynamics of the shock wave motion. Amplification of velocity fluctuations and substantial changes in length scales are the most important outcomes of interactions of shock waves with turbulence. This indicates that such interactions may greatly affect mixing. The use of shock waves, for instance, has been proposed by Budzinski, Zukoski & Marble (1992) as means to enhance mixing of fuel with oxidant in ramjets.

Turbulence amplification through shock wave interactions is a direct effect of the Rankine–Hugoniot relations when they are coupled with the downstream equations. However, this type of amplification should be decoupled from other effects which also contribute to turbulence amplification such as destabilizing streamline curvature, flow separation, dilatation effects or longitudinal pressure gradients which may be present in the flow before or after the interaction with the shock (Andreopoulos & Muck 1987; Honkan & Andreopoulos 1992).

The recent review by Andreopoulos, Agui & Briassulis (2000) has indicated that the outcomes of the shock–turbulence interaction depend on:

(i) the characteristics of the interacting shock wave, which include its strength, relative orientation to the incoming flow, and location and shape;

(ii) the state of turbulence of the incoming flow as it is characterized by the fluctuation levels of velocity, density, pressure and entropy and length scales;

(iii) the level of compressibility of the incoming flow and

(iv) the flow geometry and boundary conditions.

The present work focuses on an idealized case of an interaction of a planar shock wave travelling through grid-generated turbulence. This flow represents an interaction with a simplified yet relevant geometry, which can be used to investigate basic physics and/or as a test case for turbulence modelling in computational fluid dynamics. One way to simulate experimentally this interaction is by taking advantage of the induced flow behind a moving shock in a shock tube. This flow is passed through a turbulence-generating grid and the decaying turbulence behind the incident shock interacts with the shock wave after it has been reflected from the endwall of the shock tube.

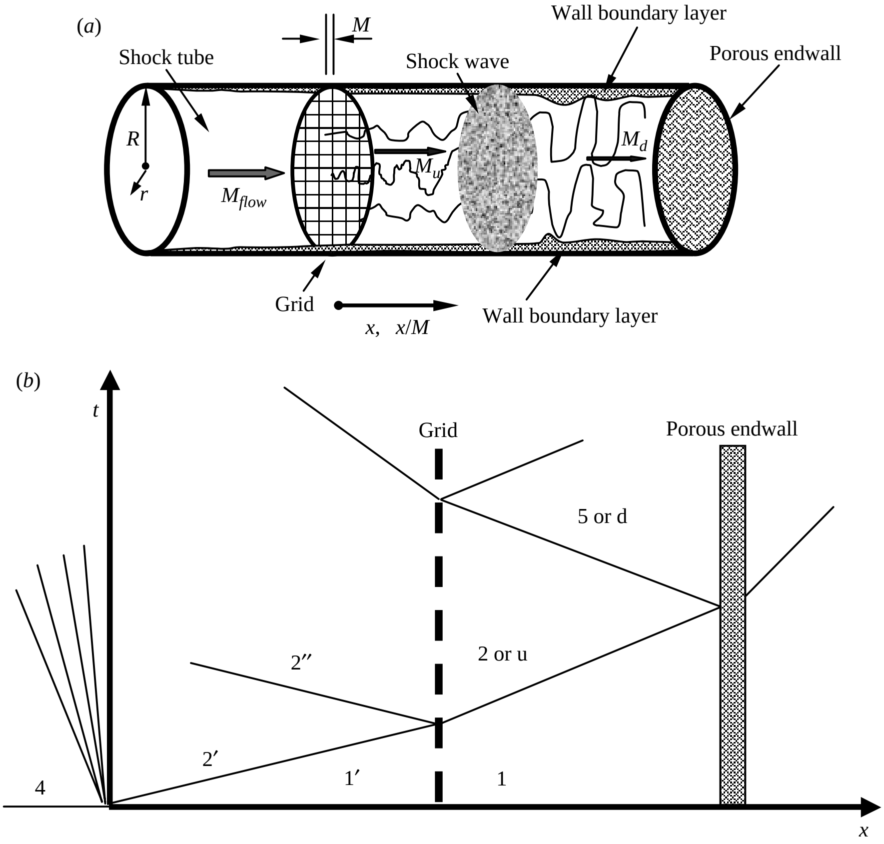

FIGURE 1. (*a*) Schematic of flow interaction. (*b*) x–t diagram of the interaction.

Figure 1(*a*) shows a schematic of the flow interaction in the shock tube. This flow configuration in the shock tube provides a platform to investigate some fundamental issues associated with the amplification of turbulence through its interaction with the moving shock wave.

A unique facility has been developed at CCNY in which the Mach number of the flow behind the reflected shock can be controlled independently of the shock wave strength to a certain extent. This has been achieved by replacing the endwall of the shock tube with a porous wall of variable porosity. The large size of this facility allows measurements of turbulence with high spatial and temporal resolution (see Briassulis & Andreopoulos 1996; Briassulis, Agui & Andreopoulos 2001; Agui 1998). Thus, shock interactions even with incompressible flows can be generated. Figure 1(*b*) depicts the wave patterns generated inside the shock tube and their reflections over various hardware components.

Previous experimental work on this type of shock wave interaction is very limited. Keller & Merzkirch (1990) measured the density fluctuations in a similar interaction between a travelling wave and the wake of a perforated plate by using speckle photography. They demonstrated that density fluctuations are considerably amplified. The experimental works of Honkan & Andreopoulos (1992) and Honkan, Watkins & Andreopoulos (1994) showed for the first time the dependence of the interaction of the shock wave with grid generated turbulence on the turbulent scales of the incoming flow. Haas & Stutervant (1987) and Hesselink & Stutervant (1988) investigated the interaction of a weak shock wave with a single discrete gaseous inhomogeneity and statistically uniform medium respectively. It was found that the shock-induced Rayleigh–Taylor instability enhances mixing considerably, and that turbulent scales seem to decrease after the passage of the shock. The latter is in contrast to previous work by Keller & Merzkirch (1990) and Debieve *et al.* (1985) and most probably is due to the Rayleigh–Taylor instability, which is as a result a nonlinear interaction of two pre-existing modes in the flow, namely, that of the vorticity mode and that of the entropy.

The shock wave from a simplistic point of view can be considered as a steep pressure gradient. Information from experiments and simulation of low-speed flows with such pressure gradients indicate that 'rapid distortion' concepts hold and, in the limit of extremely sharp gradients the nonlinearity may be ignored (Hunt 1973; Hunt & Carruthers 1990). The physics associated with the compressibility phenomena that are responsible for this amplification are not well understood. There are various issues which remain unresolved. For instance: How much of the amplification of turbulence in interactions with shock waves is due entirely to the Rankine–Hugoniot conditions? Why are small eddies amplified more than large eddies? Are the length scales of the incoming turbulence reduced or amplified through such interaction? Are the solenoidal and dilatational terms of the dissipation rate of turbulent kinetic energy also reduced? How is the velocity gradient tensor $A_{ij} = \partial U_i \partial x_j$ affected by the shock wave? Is enstrophy amplified more than turbulent kinetic energy?

The first attempt to theoretically consider the passing of a turbulent field through a shock wave is attributed to Ribner (1953, 1986) who decomposed the incident disturbance shear wave into acoustic, entropy and vorticity waves. In his linear interaction analysis (LIA) Ribner formulated the interaction of a plane vorticity wave with a shock wave as a boundary-value problem. The wavenumber vector is refracted across the shock due to the changes in thermodynamic properties and therefore diverges at a different angle from the incident. The condition that the phases should remain unchanged across the shock yields, that, upstream and downstream of the shock, the cyclic frequency and the component of the wavenumber vector parallel to the shock front are the same. Ribner's analysis obtained the first evidence of turbulence enhancement through interactions with shock waves. His predictions were verified qualitatively by Sekundov (1974) and Dosanjh & Weeks (1964). Several analytical and numerical studies of this phenomenon by Morkovin (1960), Zang, Husseini & Bushnell (1982), Anyiwo & Bushnell (1982), Rotman (1991), Lee, Lele & Moin (1993) and Hannappel & Friedrich (1995) show very similar turbulence enhancement. Chu & Kovasznay (1957) indicated that there are three fluctuating modes that are coupled and responsible for the turbulence amplification: (i) acoustic (fluctuating pressure and irrotational velocity mode); (ii) turbulence (fluctuating vorticity mode) and (iii) entropy (fluctuating temperature mode). These modes are, in general, nonlinearly coupled and the Rankine–Hugoniot jump conditions across the shock indicate that when any one of the three fluctuating modes is transferred across the shock wave it not only generates the other two but it may also considerably amplify itself. The present work focuses primarily on the turbulence and secondarily on the acoustic (pressure) fluctuation modes, since temperature fluctuations are extremely small (see Honkan *et al.* 1994). The transfer of homogeneous and isotropic turbulence across a normal shock propagating inside the flow has been studied in the present investigation. Previous work on this subject is rather limited. The reason is that it is rather difficult to experimentally setup a configuration where a decaying, grid-generated turbulence will interact with a plane shock in a wind tunnel. Debieve & Lacharme (1985), for

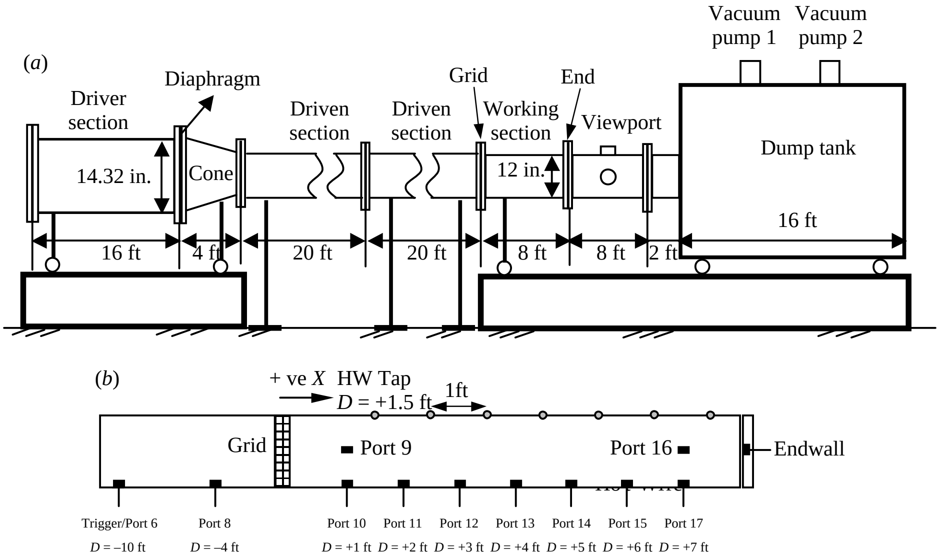

FIGURE 2. (*a*) Schematic of shock tube research facility. (*b*) Two-dimensional schematic of the working section with pressure and hot-wire tap locations along the 8 ft length.

instance, attempted to generate homogeneous and isotropic turbulence by installing a grid inside the settling chamber of a supersonic wind tunnel. The flow, however, became anisotropic after it passed through the contraction of the wind tunnel. In another attempt by Barre, Allem & Bonnet (1996) to generate shock wave interactions with isotropic turbulence a normal shock wave was formed by the interaction of two oblique shock waves of symmetrical orientation. However, the flow after the interaction was highly accelerated because of the presence of two shear layers/slip lines at the boundaries of the useful flow region.

The objective of the present research work is a better physical understanding of the interaction of a moving shock wave with the decaying turbulence. The work is a continuation of previous experiments that were carried out by Honkan & Andreopoulos (1992), and Honkan, Watkins & Andreopoulos (1994) in a small-diameter shock tube and by Briassulis *et al.* (2001) in the new high-resolution shock tube research facility of CCNY. The present paper reports the results of the measurements of the time-dependent, three-dimensional velocity and vorticity fields and full velocity gradient and strain-rate tensors during the interaction with the shock wave. These measurements, particularly those that include measurement of the full velocity gradient tensor, are extremely difficult to carry out and the results obtained are the first attempted in this type of compressible flow. The work by Xanthos, Briassulis & Andreopoulos (2002) describes the behaviour of the pressure field during the shock wave interaction with free-stream turbulence. A full description and documentation of the incoming compressible decaying turbulence before the interaction can be found in Briassulis *et al.* (2001, hereafter referred to as BAA).

2. Experimental set-up and techniques

The experiments were performed in the large-scale Shock Tube Research Facility (STURF), shown in figure 2(*a*), which is located at the Mechanical Engineering Department of CCNY. The large dimensions of this facility, 1 ft in diameter and 88 ft in length, provide an excellent platform for high-spatial-resolution measurements of turbulence with long observation time of steady flow. The induced flow behind the travelling shock wave passes through a turbulence-generating grid installed at the beginning of the working section of the facility. Several turbulence-generating grids were used at three different flow Mach numbers each. The velocity of the induced flow behind the shock wave depends on the rupture pressure of the diaphragm, i.e. driver strength P_4.

The present shock tube facility has three distinguishing features. The most significant one is the ability to control the strength of the reflected shock and the flow quality behind it by using a removable porous endwall, placed at the flange between the dump tank and the working section. The impact of shock wave on the endwall would result in a full normal shock reflection in case of zero porosity (solid wall), a weak shock reflection in case of moderate porosity, or expansion waves in case of infinite porosity (open endwall). The second feature of the facility is the ability to vary the total length of the driven section by adding or removing one of the several pieces or modules that are available or rearrange their layout. Proper arrangement of the layout of the various modules of the shock tube can maximize the duration of the useful flow. The third feature of the facility is its large diameter, which allows a large area of uniform flow in the absence of wall effects to be available while at the same time providing a platform for high spatial resolution in the measurements of turbulence.

The working (test) section is fitted with several hot-wire and pressure ports (see figure 2*b*). Thus pressure, velocity and temperature data can be acquired simultaneously at various locations downstream from the grid, therefore reducing the variance between measurements. High-frequency pressure transducers, hot-wire anemometry and Rayleigh scattering techniques for flow visualization have been used in the present investigation.

To simultaneously resolve two-dimensional velocity components with hot wires, a cross-wire (X-wire) arrangement was used. New three-wire probes were designed and custom built by AUSPEX Corp. Six different three-wire probe assemblies were used concurrently at different downstream locations, all adjustable to different lengths, each carrying two hot wires in an X configuration and one cold wire for simultaneous velocity and temperature measurements respectively. The three-wire probes were equipped with 5 μm platinum/tungsten wires for velocity measurements and with a 2.5 μm platinum/tungsten wire for temperature measurements. To eliminate any wake effects from probes located upstream, all of the probes were staggered at increasing distances from the tube wall with downstream station and reoriented by 90° every other probe by using two axial arrays of probe taps along the test section. The cross wires were driven by DANTEC anemometers model CTA56C01 and the temperature wires were connected to EG&G model 113 low-noise battery-operated pre-amplifiers/filters. The output signal of the cold wire was digitally compensated for thermal lag up to frequencies of interest. For more details on the hot-wire techniques applicable to shock tubes see Briassulis *et al.* (1995) where estimates of uncertainties in the measurements are also given.

This experimental set-up provided time-dependent measurements of two velocity components, temperature and wall pressure at several locations of the flow field simultaneously. In addition, time-dependent, three-dimensional vorticity measurements were carried out by using a new vorticity probe (see Agui 1998; BAA; Andreopoulos & Honkan (1996) and Honkan & Andreopoulos (1997).

The shock tube was fitted with nine pressure taps in the working section and eight in the driven section. Pressure transducers were placed throughout the driven section

Grid (meshes/in.)	M, mesh size (mm × mm)	Solidity, σ	M_u, Flow Mach number	Re_M	Re_λ
10 × 10	2.54	0.36	0.446	40640	NA
10 × 10	2.54	0.36	0.578	56919	NA
10 × 10	2.54	0.36	0.623	62285	NA
8 × 8	3.175	0.36	0.371	37138	162
8 × 8	3.175	0.36	0.461	53506	195
8 × 8	3.175	0.36	0.592	63458	246
5 × 5	5.1 × 5.1	0.37	0.371	59654	160–318
5 × 5	5.1 × 5.1	0.37	0.477	86315	200–269
5 × 5	5.1 × 5.1	0.37	0.576	102421	240–458
4 × 4	6.35 × 6.35	0.44	0.354	68208	213–401
4 × 4	6.35 × 6.35	0.44	0.446	105389	198–336
4 × 4	6.35 × 6.35	0.44	0.594	132921	113–352
3 × 3	8.5 × 8.5	0.39	0.321	81687	154–239
3 × 3	8.5 × 8.5	0.39	0.474	124203	184–201
3 × 3	8.5 × 8.5	0.39	0.564	215043	330–747
2 × 2	12.7 × 12.7	0.28	0.346	137319	186–281
2 × 2	12.7 × 12.7	0.28	0.436	169025	195–452
2 × 2	12.7 × 12.7	0.28	0.592	261667	560–1331
1.33 × 1.33	19.05 × 19.05	0.26	0.368	200371	210–278
1.33 × 1.33	19.05 × 19.05	0.26	0.504	295721	217–612
1.33 × 1.33	19.05 × 19.05	0.26	0.607	398661	257–760

TABLE 1. Bulk flow parameters of the experiments performed.

in order to monitor the passage of the shock wave and also to check its uniformity through the driven section. For the present experiments, high-frequency-response Kulite pressure transducers type XCQ-062 were installed in the shock tube at various locations, so that wall pressure fluctuations can be measured simultaneously as a function of time. The shock tube was pressurized so any leaks can be detected, as well as to calibrate the pressure transducers. The shock tube was free of leaks and the static response of the transducers was found to be linear. Aluminium plates were used as diaphragms and were placed in between the driver and the conical sections.

A detailed description of the facility and the results of the qualification tests can be found in Briassulis (1996) and Briassulis *et al.* (1996).

During each experiment all signals were acquired simultaneously with the ADTEK data acquisition system. The ADTEK AD830 board is a 12-bit EISA data acquisition system, capable of sampling simultaneously eight channels at 333 kHz each channel. Three of those boards were available providing 24 simultaneous sampled channels at 333 kHz per channel. It should be mentioned that no sample-and-hold units were used in the present data acquisition since each channel was dedicated to an individual analog to digital converter. The data acquisition system was triggered by the arrival of the shock wave at the location of a wall pressure transducer 3.30 m upstream of the grid. The grid was installed at the beginning of the working section.

The bulk flow parameters of the experiments performed are summarized in table 1 and include the grid mesh density, the mesh size M, the flow Mach number M_2 behind the incident shock of strength M_I, the Reynolds number based on mesh size Re_M and mean flow velocity U_1, the strength of the reflected shock M_R and the solidity of the grids σ, defined as the projected solid area per unit total area so that $\sigma = 1 - [1 - d/M]^2$ where d is the rod diameter. All grids were fabricated from circular steel rods.

The values of M_2 were obtained in the flow downstream of the grid and they are slightly smaller than the Mach number values obtained in the approaching flow upstream of the grid (BAA). As the incoming shock wave reaches the grid, it is transmitted through the grid with some minor losses due to viscous effects while a very weak reflected shock travels as a small disturbance in the opposite direction upstream as a result of the impact of the incident shock on the grid. This disturbance is stronger at higher shock Mach numbers and in impacts with higher solidity grids. This weakly reflected shock reduces the velocity and increases the temperature of the approaching flow by small amounts respectively. The induced flow behind the incident shock, after it has experienced the effects of the upstream travelling weakly reflected shock, passes through the grid to form a nearly homogeneous and isotropic flow.

3. Vorticity measurements

A new multi-hot-wire probe has been developed which is capable of measuring velocity-gradient-related quantities in non-isothermal flows or in compressible flows. The present probe has been build using the experience gained with vorticity measurements in incompressible flows (see Honkan & Andreopoulos 1997) by using a probe with nine wires, and with velocity measurements in compressible flows by using single and cross-wire probes (see Briassulis *et al.* 1995). The present vorticity probe, which consists of 12 wires, is a modification of the original design with nine wires by Honkan & Andreopoulos (1997). The three additional wires were operated in the so-called constant current mode and used to measure time-dependent total temperature.

Since the probe essentially consists of a set of three modules or arrays (see figure 3*a–c*) it is necessary to provide several key features of the individual hot-wire modules. Each module contains three hot wires operated in the constant-temperature mode (CTM) and one cold-wire sensor operated in the constant-current mode (CCM). Each wire of the triple-wire sub-module is mutually orthogonal to the others, thus oriented at 54.7° to the probe axis. Each of the 5 μm diameter tungsten sensors is welded on two individual prongs, which have been tapered at the tips. Each sensor is operated independently since no common prongs are used. Each of the 2.5 μm diameter cold wires was located on the outer part of the sub-module.

Details of the techniques associated with the use of triple-wire arrays can be found in Andreopoulos (1983*a*) while estimates of errors related to probe geometry and turbulence intensity are described by Andreopoulos (1983*b*).

Extensive testing of the probe has been carried to assess its performance in shock tube flows. The reader is referred to BAA for details of the tests and the techniques associated with the use of the probe. The probe was also tested in low-speed incompressible boundary layer flows where vorticity measurements have been obtained in the past with a nine-wire probe (see Honkan & Andreopoulos 1997) and with optical techniques (see Agui & Andreopoulos 2003). Comparison of the data obtained with the new probe with these previous measurements was very satisfactory. This provided considerable confidence in the use of the probe in weakly compressible grid-generated turbulence, described by BAA, and in flows with shock interactions like the present one.

Velocity calibrations were carried out inside the shock tube by firing the tube at various pressures corresponding to Mach numbers anticipated to be found in the flows under investigation. Yaw and pitch calibration of the probe was also carried out *in-situ*.

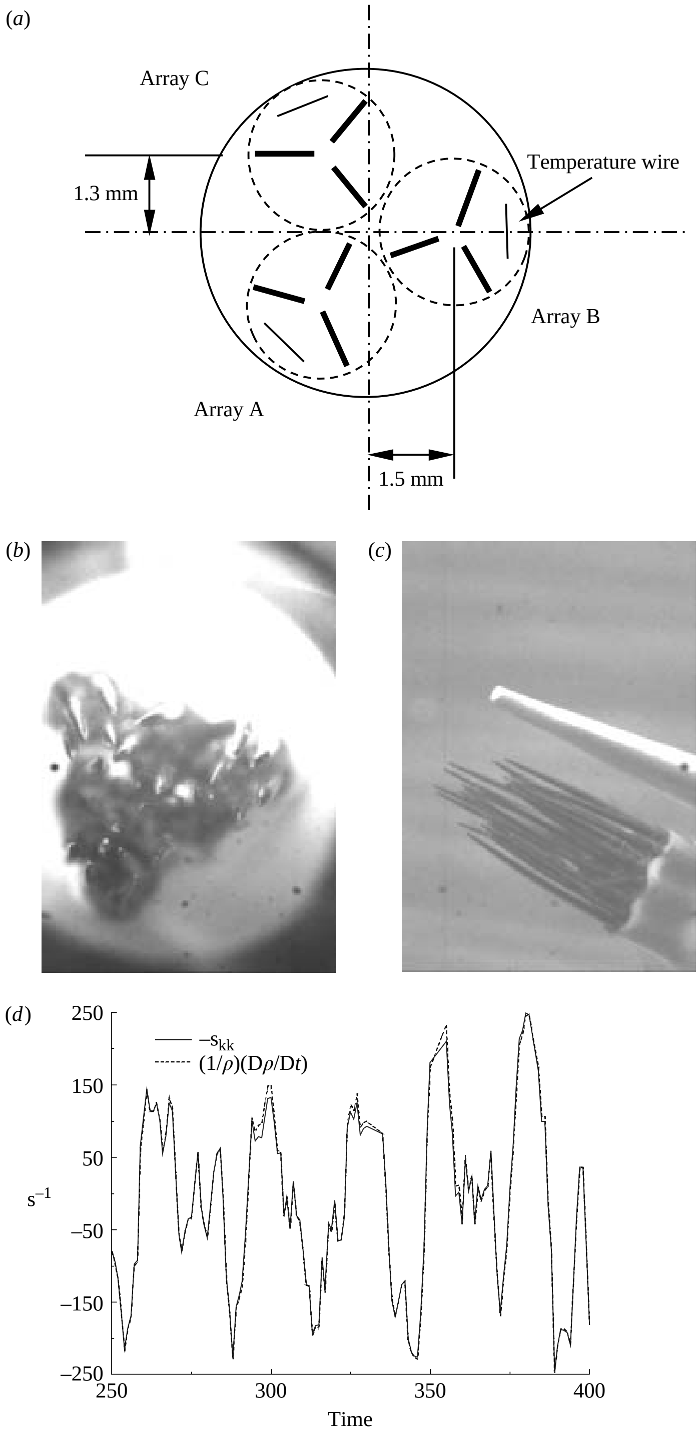

FIGURE 3. Vorticity probe: (*a*) probe sensor geometry and arrays, (*b*) photograph showing comparison with toothpick, (*c*) close-up view directly into the probe. (*d*) Comparison of two dilatation signals.

No.	Grid	x/M	M_u	U_1 ($\mathrm{m\,s^{-1}}$)	ρ ($\mathrm{kg\,m^{-3}}$)	P (kPa)
1	2×2	48	0.308	121	1.59	155
2	2×2	48	0.388	151	1.74	174
3	3×3	72	0.362	139	1.7	170
4	3×3	72	0.425	161	1.84	188

TABLE 2. Bulk flow parameters in vorticity measurements.

The digitized signals were processed off-line. The cold-wire signals were first converted to total temperature, which together with the hot-wire signals were used to obtain instantaneous three-dimensional mass fluxes at three neighbouring locations within the probe. Numerical techniques and algorithms used in the computations of velocity gradients were very similar to those described by Honkan & Andreopoulos (1997). The only difference is that in the present case mass fluxes and their gradients were computed at the centroid of each module instead of velocities and velocity gradients.

Mass fluxes were further separated into density and velocity by using the method adopted by Briassulis *et al.* (1996). Decoupling density from mass fluxes assumes that static pressure fluctuations are small. This is the so-called 'weak' version of the original 'strong Reynolds analogy' hypothesis of Morkovin (1960). The original hypothesis is based on the assumption that pressure and total temperature fluctuations are very small. In the present work, total temperature was measured directly and therefore no corresponding assumptions were needed. The pressure, however, was measured at the wall and not at the location of the hot-wire measurement. The mean value of this pressure signal was used to separate the density and velocity signals since no mean pressure variation has been detected across a given section of the flow. The procedure involves an expression for mass flux, m_i, in terms of total temperature, T_0, and pressure, p, at the centroid of each array:

$$m_i = \rho U_i = pU_i/RT = pU_i/[R(T_0 - U_k U_k/2c_p)],$$

where U_i is the instantaneous velocity component, $i = 1, 2$ or 3 and $U_k U_k = U_1^2 + U_2^2 + U_3^2$. The velocity can be decomposed into $U_i = \bar{U}_i + u_i$. An iterative scheme was used to decouple density and velocity.

In summary, it should be emphasized that the major contribution of the present hot-wire techniques is the addition of temperature wires to obtain instantaneous information on total temperature. This allowed decoupling of all partial sensitivities of the probe from each other. Thus,

$$S_\rho = \partial E/\partial\rho \neq S_{\rho u} = \partial E/\partial\rho u \neq S_u = \partial E/\partial u,$$

where E is the voltage output from the probe.

Four additional experiments were carried out with the new multi-wire vorticity probe. Table 2 shows the bulk flow parameters of the experiments, which were performed at two different flow Mach numbers and with two different grids.

The present vorticity probe was capable of measuring the full rate-of-strain and rate-of-rotation tensors, S_{ij} and R_{ij} respectively, as well density gradients with high temporal and spatial resolution upstream and downstream of the shock wave flow fields. In order to demonstrate the capabilities of the present probe and provide information about its accuracy the dilatation term $S_{kk} = (1/\rho)\mathrm{D}\rho/\mathrm{D}t$ has been computed by two different methods from the present data. In the first method S_{kk} has been computed from the velocity gradients information. The second method involved the estimation of dilatation from the density information to compute $(1/\rho)\mathrm{D}\rho/\mathrm{D}t$. A comparison of the data obtained by these two methods is shown in figure 3(*d*) where the two signals are plotted. The overall agreement between the two signals appears to be very good. There are occasional differences between the two signals, particularly around the peaks, of no more than 7%. This difference, however, has no effect on the overall statistics.

4. The shock tube flow

Unlike conventional low-speed grid turbulence, generated in a wind tunnel, the present flow is produced in a shock tube behind a moving shock wave. Shock tubes are traditionally used to study mainly moving shock waves and their reflections or interactions with solid surfaces and to generate high-temperature environments. Our work is not the first one to configure a stationary flow behind a moving shock wave. There have been several attempts in the past to utilize the induced flow behind the shock to study several flow phenomena.

The formation of a nearly homogeneous and isotropic turbulent flow with decaying intensity can be described by considering the time-dependent signals of the three velocity components shown in figure 4(*a*). The signals shown in this figure were obtained by the vorticity probe at $x/M = 72$ downstream of the 3×3 grid with solidity $\sigma = 0.39$. As the incoming shock reaches the grid, it is partly transmitted through the grid with some minor losses of its strength associated with viscous effects, and it is partly reflected and it travels in the opposite direction. The work by Xanthos *et al.* (2003) provides a more detailed account of the interaction of the shock wave with the grid and the pressure losses measured during its transmission through the grid.

The transmitted incident shock propagates downstream and the probe detects it as is indicated by the sudden rise in the longitudinal velocity component U_1. The induced flow behind the incident shock, after it has experienced the effects of the upstream travelling weakly reflected shock off the grid, passes through the grid to form a nearly homogeneous and nearly isotropic flow.

The incident shock travels downstream and is reflected off the porous endwall and returns to the measuring location to interact with the decaying turbulence present in the induced flow behind the incident shock. The reflected shock, which travels in the upstream direction, reduces the velocity and increases the temperature of the approaching flow initially induced by the incident shock. This is evident in the longitudinal velocity component shown in figure 4(*a*). The lateral velocity components, U_2 and U_3, which are parallel to the shock front, experience no change in their mean value with the arrival of the reflected shock.

The duration of the useful induced flow behind the shock wave in the present hardware configuration of the various components of the shock tube may be limited by the arrival of reflected expansion waves from the driver endwall which are formed during the rupture of the diaphragm and the arrival of the contact surface which is characterized by a large temperature gradient. The longitudinal velocity signal in figure 4(*a*) also shows the arrival of the expansion waves, which decrease the velocity of the flow gradually.

Statistical averages were obtained from the quasi-stationary signal before and after the arrival of the reflected shock off the endwall. The signals were first inspected to detect the presence of undesirable grid shocks or expansion waves within the useful duration of the signals as well as for their stationarity. The signals displayed a relatively slow growth of the ensemble mean values with time, indicating that the flow

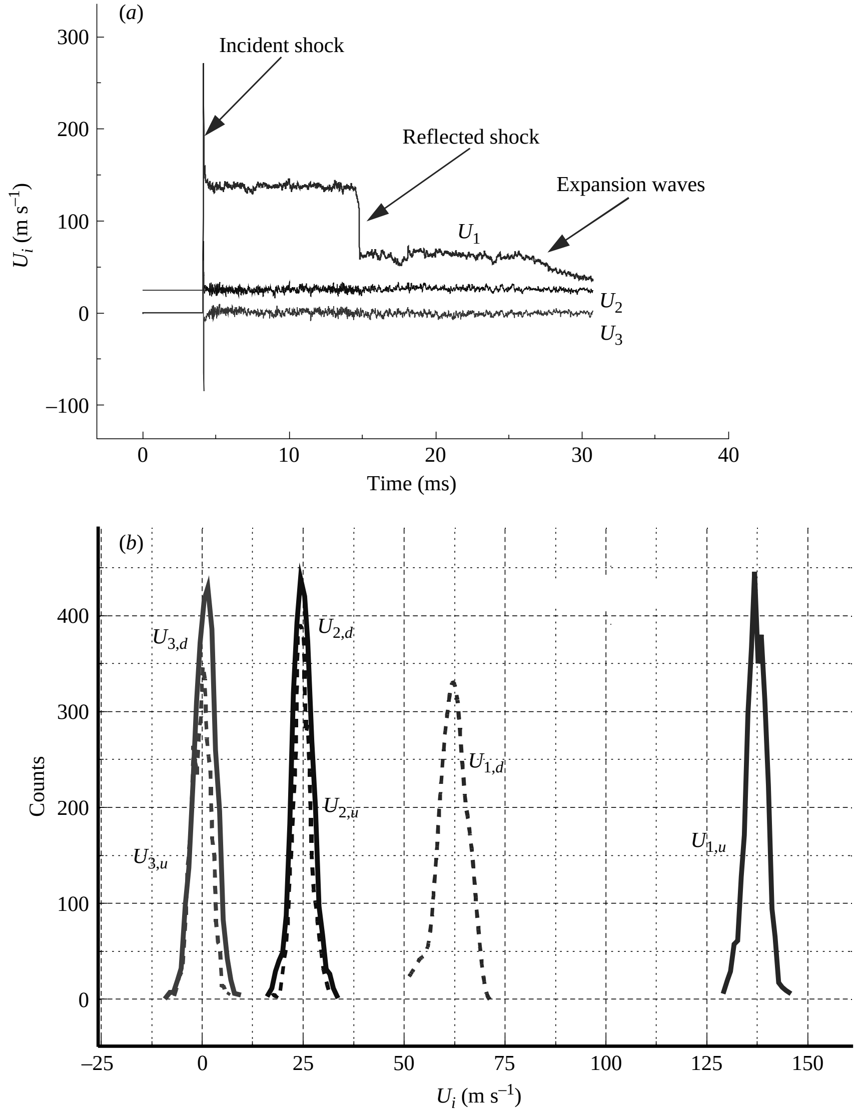

FIGURE 4. (*a*) Time-dependent signals of three velocity components. (*b*) Histograms of the velocity components upstream (solid lines) and downstream (dashed lines) of the interaction. Values of U_2 have been displaced by 25 m s^{-1}.

could be considered stationary. The reader is referred to BAA for a detailed description of the techniques used to obtain reliable statistics from the time-dependent data.

An extensive program has been undertaken to assess the quality of the grid flow established in the shock tube. This was accomplished by measuring the flow uniformity and homogeneity in the working section on planes normal to the flow and in the longitudinal direction. The flow isotropy was also tested and verified by several different methods. Results and details of the flow quality are shown and discussed by BAA. They have indicated that flow homogeneity is better in fine grids than in coarse ones.

Typical results obtained in the present investigation are shown in figure 4(*b*) where histograms of the values of the three velocity components upstream of the shock,

$U_{1,u}$, $U_{2,u}$, $U_{3,u}$ and downstream of the shock $U_{1,d}$, $U_{2,d}$, $U_{3,d}$ are plotted. The range of fluctuations appears to be the same in all of the three velocity components before the interaction as expected in an isotropic flow. As a result of the interaction, however, turbulence characteristics change. Longitudinal velocity fluctuations increase while lateral velocity fluctuations are slightly reduced.

To conclude this section, it appears that the flow established in the shock tube is invariant to translation and rotation since its quality, in terms of uniformity of statistical averages, and isotropy is very good.

5. Uncertainty estimates

The pressure and total temperature measurements depend directly, through obtained calibration constants, on the raw voltage data from the individual sensors. These probes because of their linear response produced two calibration constants, sensitivity and d.c. offset. Therefore estimates of the uncertainty in the measurements of pressure and total temperature acquired through a 12-bit A/D converter depended mostly on the bit resolution and the residual errors from the calibration constants. Uncertainties in the range of less than 0.5% in pressure and about 2% in total temperature were found for typical measurements of these two quantities.

The mass flux measurements were tied to significantly more complex relations, which depended on the individual and relative geometry of different sensors. Mass flux was found to depend on the following variables: captured raw voltage E_i, reference temperature T_r, total temperature T_o, wire temperature T_w, calibration constants and yaw or pitch coefficients. Estimates of the uncertainty in the measurements of mass flux after considering all the above contributing factors was found to be between 1% and 3%. Uncertainty values for the velocity were estimated to be between 1.5% and 3.5%. In obtaining all these estimates the square root of the squares of all partial uncertainties involved was assumed to model the error propagation into the final results. MATHCAD was used to calculate the partial uncertainties.

Following the work of BAA estimates of the uncertainties associated with the measurements of velocity gradients were also obtained by considering the propagation of the uncertainties in the measurement of each quantity involved in the process. A typical velocity gradient is measured through the following approximation:

$$\partial U_i/\partial x_j \approx (U_2 - U_1)/l_p = F$$

where U_2 and U_1 are the velocities at two nearby locations, and l_p is the distance between these locations. If the uncertainties in the measurements of U_2 and U_1 are the same, $\Delta U_1 = \Delta U_2 = \Delta U$, and l_p is determined accurately, then the relative uncertainty $\Delta F/F$ will be given by:

$$\Delta F/F = \{2[\Delta U/(U_2 - U_1)]^2\}^{1/2}$$

A typical ΔU is 2% of mean U, which corresponds to about $2\,\mathrm{m\,s^{-1}}$ while typical velocity differences $U_2 - U_1$ can be up to six times the r.m.s. value, u'. If a typical value of this velocity difference is assumed of about $30\,\mathrm{m\,s^{-1}}$ in the near field of the grid and $15\,\mathrm{m\,s^{-1}}$ further downstream, then the uncertainty $\Delta F/F$ appears to be 10% in the near field and 14% in the far field.

Lower uncertainty estimates have been found if the relation $\partial U_i/\partial x_j \approx u'/\lambda = F$ is used for their computation. In this case the relative error is

$$\Delta F/F = \{(\Delta u'/u')^2 + (\Delta\lambda/\lambda)^2\}^{1/2}$$

where λ is Taylor's microscale. For a typical relative error in u' of 5% and 10% in λ the relative error appears to be about 11%. It should be note that the relative error $\Delta F/F$ increases as the distance away from the grid increases because the absolute value of F decreases.

Finally the finite number of statistically independent events considered in the data analysis of certain flow cases introduces an uncertainty in the statistical results. Computations of the integral time scale, L_t from auto-correlation functions $R_{uu}(\tau)$ indicated that the number of independent samples in general was between 200 and 400. Downstream of the interaction, time scales L_t increase and the number of statistically independent events is reduced. In addition, the duration of the useful data upstream of the shock is shortened at locations close to the porous endwall because the reflected shock wave arrives earlier than at locations close to the grid. The start of the useful data corresponding to the flow upstream of the incident shock is also delayed by the passage time of the originally stagnant air mass between of the grid and the measuring location. This air is downstream of the grid when the incident shock wave passes and therefore the corresponding induced flow does not pass through the grid. The number of independent samples in these cases was about $N \simeq 60$–100. Bendat & Piersol (2000) indicate that the relative error in the estimate of the variance of the velocity fluctuations is $2/N$, which for this specific case at large x/M is between 2% and 4%. It should be noted that N depends on the shape of R_{uu}, consequently N can be extended to large values if low-frequency disturbances are present in the flow field, which are not related to the actual flow turbulence. If high-pass filtering at 200–400 Hz is applied to the present data L_t is reduced substantially and N increases by a factor of 2. No such filtering has been applied to the present data other than what is imposed by the record length. For a 10 ms record length the lowest frequency of interest is about 100 Hz.

Another direct piece of evidence of the adequacy of statistical samples can be provided by the rate of convergence of the various statistical quantities, which are computed in the present data analysis. As was shown in BAA, estimates of the convergence uncertainties observed in the present analysis indicate an error of less than 3%. This error is substantially less at higher Mach numbers and closer the grid locations.

The spatial resolution of the probe is between 0.6λ and 3λ upstream of the shock region and 0.3λ and λ in the downstream region. The resolution expressed in Kolmogorov's viscous scale $\eta = (\nu^{3/4}/\varepsilon)^{1/4}$ appears to be in the range between 3η and 30η. In that respect the expected attenuation of the measurement of vorticity r.m.s. due to limited spatial resolution is not very significant.

6. The decay of isotropic turbulence

Three characteristic regions can be found in the flow behind a turbulence-generating grid. First is the developing region close to the grid where rod wakes are merging and production of turbulent kinetic energy takes place. This region is followed by one where the flow is nearly homogeneous and isotropic but where appreciable energy transfer from one wavenumber to another occurs. This region is best described by the power-law decay of velocity fluctuations

$$\frac{\bar{u}^2}{U^2} = A\left[\frac{x}{M} - \frac{x_0}{M}\right]^{-n} \tag{6.1}$$

where A is the decay coefficient, $(x/M)_0$ is the virtual origin, n is the decay exponent. The third region or final region of decay is the farthest downstream of the grid and is dominated by strong viscous effects acting directly on the large-energy-containing eddies.

The turbulent or fluctuation Mach number, $M_t = q_t/\bar{c}$ with $q_t = \overline{(u_i u_i)}^{1/2}$ and c the speed of sound, seems to be the most appropriate parameter describing compressible turbulence. It was shown in BAA that Mach number fluctuations in weakly compressible turbulence decay according to the power law

$$M_t^2 = B\left[\frac{x}{M} - \frac{x_0}{M}\right]^{-n} \tag{6.2}$$

where $B = 3AM_u^2$.

In flows where turbulence is distorted by a rapidly applied strain, like the strain $S_{11} = (\partial U_1/\partial x_1)_{sw}$ in the present case across the shock wave, the dissipative time scale of turbulence or eddy turnover time $T_\varepsilon = L_\varepsilon/q$, where L_ε is the dissipation length scale and $q = (1/2q_t^2)^{1/2}$, should be directly compared to the time scale of the applied strain $T_{sw} = 1/S_{11}$.

The dissipation length scale, L_ε, is defined as $L_\varepsilon = q^3/\varepsilon$, where ε is the dissipation rate of turbulent kinetic energy q^2. The time T_t then appears to be $T_t = q^2/\varepsilon$. This time scale indicates how fast the kinetic energy of a typical turbulent eddy is dissipated into heat. According to equation (6.1) q^2 decays as $[x - x_0]^{-n}$ and therefore ε varies as $[x - x_0]^{-n-1}$. Under these circumstances T_t is proportional to $[x - x_0]$, i.e.

$$T_t\frac{U}{M} = \frac{q^2}{\varepsilon}\frac{U}{M} = \frac{1}{n}\left[\frac{x}{M} - \frac{x_0}{M}\right]. \tag{6.3}$$

If it is assumed that turbulent eddies are convected by the mean velocity U then $x = Ut$ and the (6.3) becomes

$$T_t = \frac{q^2}{\varepsilon} = \frac{1}{n}[t - t_0]$$

which suggests that the eddy turnover time is proportional to the time of (6.3) convection.

A typical decay of velocity fluctuations, as fitted by the power law of equation (6.1), for the 5.08 mm mesh size grid and the corresponding dissipation rate are shown in figures 5(*a*) and 5(*b*) respectively. The corresponding eddy turnover time T_t is shown in figure 5(*c*). The velocity fluctuations and the dissipation rate are higher at higher upstream flow Mach numbers that also correspond to higher Re_M. These effects cannot simply be attributed to the increase of the mean Mach number and the associated compressibility effects of the flow but also to the increase of Re_M. Although Mach number and Reynolds number are two different independent variables they may cause quite similar effects on the flow, which may be difficult and sometimes impossible to distinguish clearly from each other. The work of BAA has shown that Re_M effects are of about the same order of magnitude and of the same sign as Mach number effects at low Mach numbers and low Re_M. They diminish gradually as M_u and Re_M increase. Thus, in most of the cases, compressibility effects prevail over Reynolds number effects at high M_u and high Re_M.

The non-dimensional data of q^2/ε shown in figure 5(*c*) clearly follow the linear dependence on x/M that is given by equation (6.3). It appears that T_t increases at locations downstream of the grid. The slope of each of these straight lines is not the same at different Mach umbers. However, the response of these data to increasing M_u is not quite obvious. The slope as shown by (6.3) is the inverse of the decay exponent n appearing in equation (6.1), which mainly depends on M_u and Re_M or grid solidity

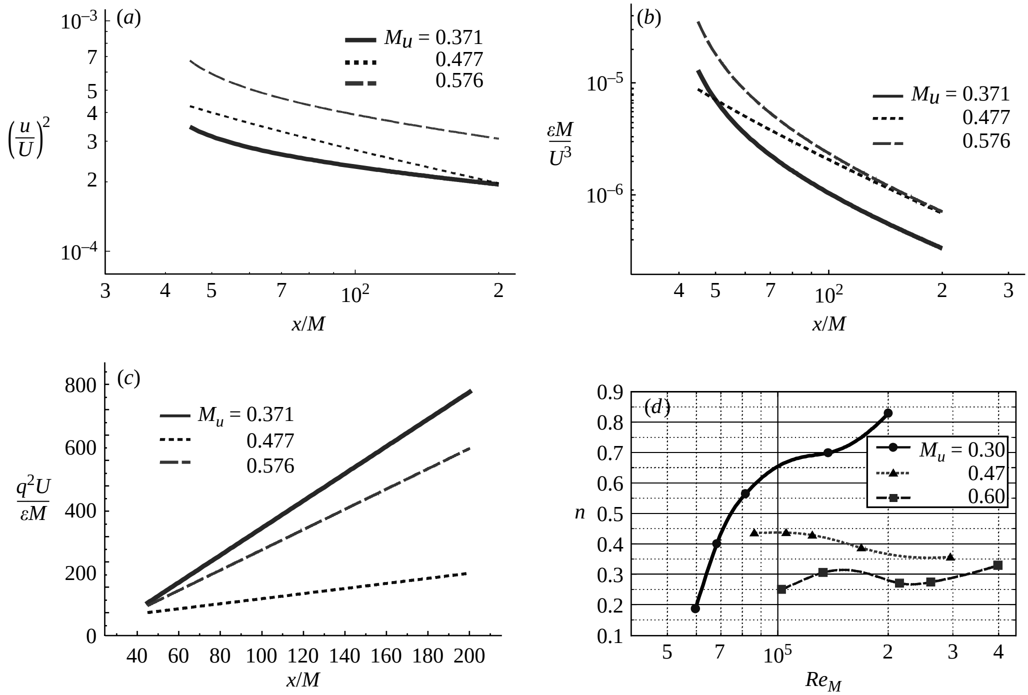

FIGURE 5. (a) Decay of longitudinal velocity fluctuations, (b) dissipation rate of turbulent kinetic energy, (c) non-dimensional dissipative time for various Mach numbers in the case of grid with $M = 5.08$ mm. (d) Decay exponent n vs. Re_M for various Mach numbers.

σ. The data of n obtained in BAA are re-plotted in figure 5(d). Values of n show very weak dependence on Re_M at $M_u = 0.47$ and 0.6. The strongest dependence of n on Re_M is evident at the lowest $M_u = 0.3$. The values of n corresponding to Mach numbers 0.3, 0.47 and 0.6 are 0.18, 0.43 and 0.25 respectively. A comparison of the inverse of these values, i.e., 5.5, 2.3 and 4, with the slopes of the straight lines shown in figure 5(c) shows agreement between the corresponding data, a fact that indicates consistency among the present results. These data also explain the effect of M_u on q^2/ε. At values of M_u larger than 0.3, q^2/ε increases with increasing M_u. This trend cannot be extended to the low-M_u case, most probably because of the difference in Re_M. The data of n in figure 5(d) also suggest that at fixed Reynolds numbers, n decreases with increasing M_u and therefore q^2/ε increases with increasing M_u at constant Re_M. This is definitely true for $Re_M > 10^5$, possibly for $Re_M > 0.87 \times 10^5$.

Inferences of the effect of Re_M on q^2/ε at constant M_u can be obtained by considering the dependence of n on Re_M at fixed values of M_u as shown in figure 5(d). It appears that q^2/ε decreases with increasing Re_M at $M_u = 0.3$. However, the effect of solidity of the grid σ on n and consequently also on q^2/ε is not clear. If the first point at the lowest Re_M is excluded then n decreases with increasing solidity, which indicates that q^2/ε increases with increasing σ at $M_u = 0.3$. At higher M_u the data suggest that q^2/ε does not really depend strongly on σ or Re_M.

The strain rate S_{11} that is associated with the imposed disturbance of the incoming shock wave can be approximated by

$$S_{11} = \left[\frac{\partial U_1}{\partial x_1}\right]_{sw} \approx \frac{|\Delta U_s|}{\Delta x_s}$$

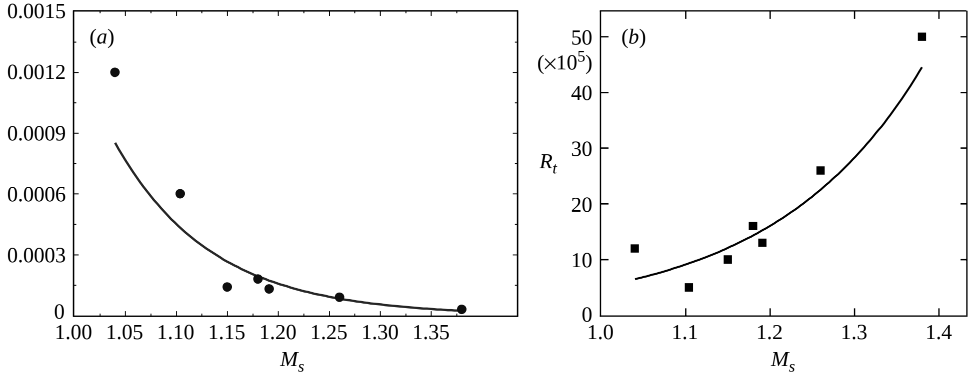

FIGURE 6. (*a*) Time scales associated with strain rates across the shock wave and (*b*) ratio of time scales $R_t = T_\varepsilon / T_{sw}$ in the present investigation.

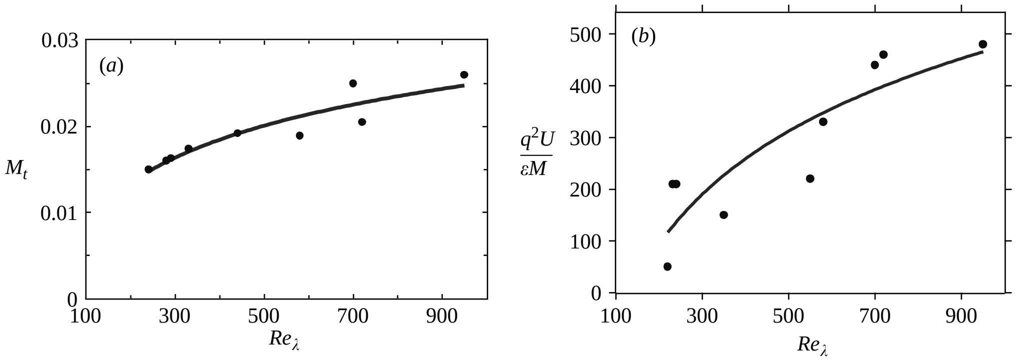

FIGURE 7. (*a*) Typical turbulent Mach number fluctuations and (*b*) typical eddy-turnover time scales against Re_λ.

where ΔU_s is the velocity difference across the shock wave and Δx_s is the shock wave thickness. An estimate of the shock wave thickness can be obtained according to Thomson (1972) and typical values of the associated time scale, $1/S_{11}$, normalized by the upstream velocity U and the mesh size of the grid M are plotted vs. M_s in figure 6(*a*). M_s is the Mach number of the interacting shock wave which in the present case is the reflected shock. The data indicate an exponential decrease of the normalized time scale T_{sw} with increasing M_s.

The ratio of two time scales $R_t = T_t / T_{sw}$ is plotted vs. M_s in figure 6(*b*). It appears that R_t grows exponentially with M_s, which is most probably due to the exponential decrease of T_{sw} with M_s rather than the weak increase of T_t with M_s. The data in figure 6(*b*) also show that the eddy turnover time T_t is about 10^6 greater than the time scale of the interaction T_{sw}. In flows like the present one where this ratio R_t reaches large values, the inviscid rapid distortion theory (RDT) and its extension to shock wave interactions (Debieve *et al.* 1985; Jacquin, Cambon & Blin 1993) may be invoked to determine several bulk characteristics of the interaction.

Figure 7(*a*) shows a typical variation of the Mach number fluctuations obtained in the present investigation with Re_λ at $x/M = 80$, a location where turbulence appears to be homogeneous and isotropic in all experiments carried out at various mean flow Mach numbers M_u. M_t and Re_λ are two independent variables used frequently in DNS to characterize the isotropic turbulence instead of M_t and Re_M, which are used mostly in experimental research where grids are used to generate isotropic turbulence. The present data demonstrate a general trend showing that Mach number fluctuations increase with increasing Re_λ, a finding that has also been supported by DNS observations.

Finally figure 7(*b*) shows typical values of the turbulent eddy turnover time T_t obtained in the present work at $x/M = 80$ for various values of Re_λ. The data indicate that the normalized T_t increases rather fast with increasing Re_λ.

7. Mach number fluctuations

The experimental work of BAA has established the validity of the decay law of Mach number fluctuations in the compressible flow upstream of the shock as described by equation (6.2). It has also been found that M_t increases with increasing M_u. After the passage of the shock the flow field changes. Velocity fluctuations in the longitudinal direction increase and Mach number fluctuations are also changed but not very drastically because the amplification of velocity fluctuations in the longitudinal direction is offset by an increase in mean temperature due to the compression. Thus M_t after the interaction is sometimes higher and sometimes lower than that before the interaction.

Figure 8(*a*) shows the results of three experiments with the 2×2 grid with $M = 12.7$ mm. Values of M_t downstream of the interaction appear to be higher than the corresponding values upstream. The increase in M_t depends on the incoming upstream flow and the strength of the interaction, i.e. the Mach number of the shock wave M_s. It appears that it is larger in interactions with stronger shock waves. The case of the 3×3 grid with $M = 8.5$ mm, shown in figure 8(*b*), however, is different. M_t is reduced during the weakest and strongest of the three interactions while it is increased during the other one.

In all experiments, the decay of Mach number fluctuations downstream of the interaction was found to follow a power law similar to that describing M_t in the upstream flow region

$$M_{t,d}^2 = B_d \left[\frac{x}{M} - \frac{x_{0,d}}{M} \right]^{-n_d}. \tag{7.1}$$

Determination of the virtual origin $(x/M)_{0,d}$, decay exponent n_d and decay coefficient B_d was accomplished by fitting the experimental data to the power law so that the residual deviation from the original data is minimized. In this way all variables were determined concurrently under the condition of minimum deviation. In that respect this approach represents a departure from previous practice where only two of the three parameters were determined through a best-fit procedure while the third one was fixed. An exception to this past practice is the work of Mohamed & LaRue (1990). A consequence of this approach is that n can reach any positive value and not only values >1 as usually is the case in previous works.

It should be emphasized that the applicability of the empirical power-law decay does not necessarily imply isotropy. The flow downstream of the shock wave is the outcome of the interaction of an isotropic turbulent flow with an axisymmetric disturbance. As a result some anisotropy in the flow is expected, at least in the initial stages following the interaction before the return to isotropy.

The present work documents the effects of the mesh size/mesh Reynolds number as well as the interaction parameters on the above mentioned quantities B_d, $(x/M)_{0,d}$,

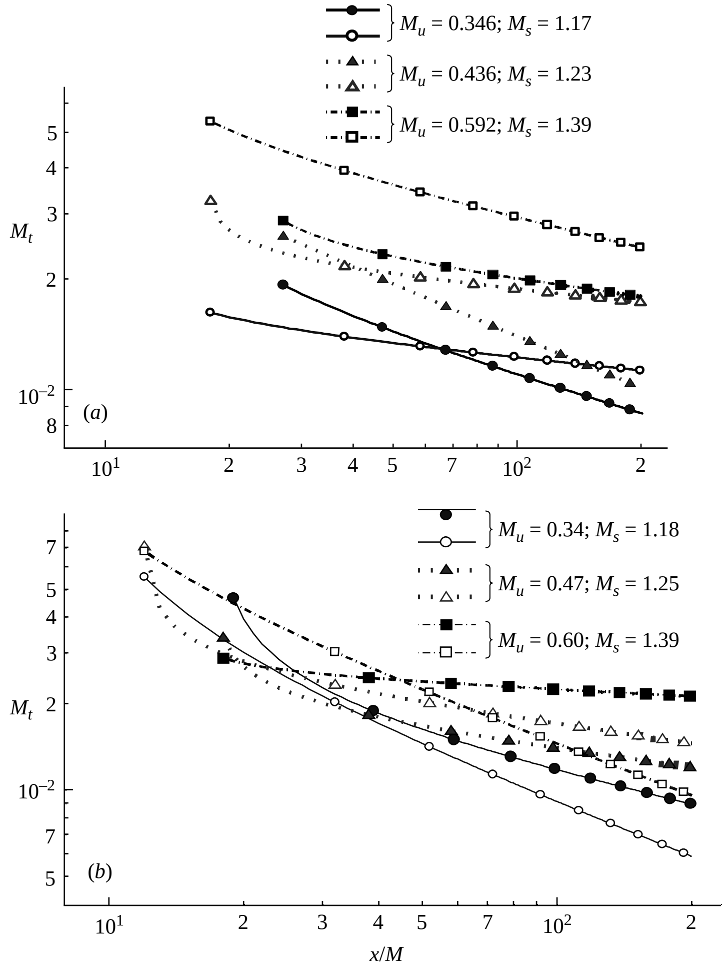

FIGURE 8. Mach number fluctuations for various experiments with the (*a*) 2×2 grid with $M = 12.7$ mm and (*b*) the 3×3 grid with $M = 8.5$ mm. Filled symbols, upstream of the interaction; open symbols, downstream of the interaction.

and n_d. Figure 9(*a*) shows a typical variation of the decay exponent, n, before and after the interaction with the shock wave of $M_s = 1.25$ for various mesh sizes of grids. The data indicate that both exponents n_u and n_d decrease with increasing mesh size M. The data shown in figure 9(*a*) are plotted in figure 9(*b*) against the solidity of each grid σ. Values of n_u and n_d appear to increase with increasing with σ. The present results show that the exponent n depends on the mesh size and solidity of the grids, i.e. initial conditions before the interaction, and that these values of n are substantially less than one. The effect of the shock interaction is very substantial since it changes the values of n and it depends on the M_s, M_u and initial conditions.

Figure 9(*c*) presents the ratio of the decay coefficient after the interaction with the shock to that before the interaction, n_d/n_u. It can be seen that this ratio is always greater than one for all investigated cases. In the weakest interactions this ratio appears to be independent of Re_M. In the cases of stronger interactions this ratio is Re_M dependent. Thus n_d/n_u depends on initial conditions, flow Mach number M_u and shock strength M_s.

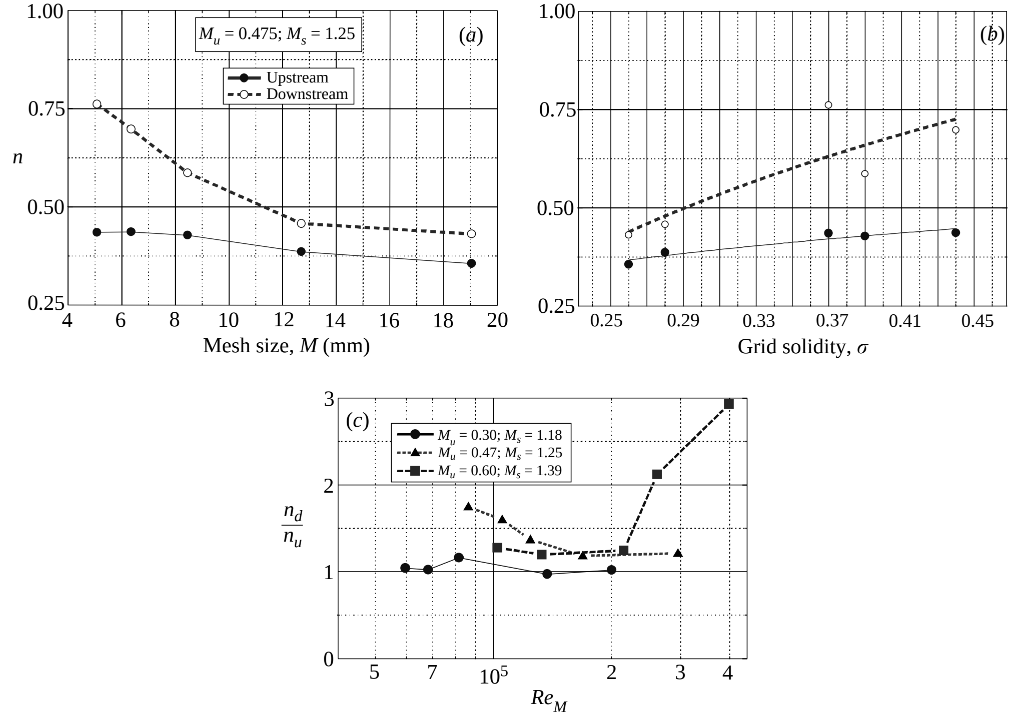

FIGURE 9. Decay exponent before and after the interaction against: (*a*) mesh size of grids; (*b*) grid solidity, (*c*) Reynolds number.

8. The thermodynamic state of turbulence

DNS and LIA work has shown in the past that the thermodynamic properties of the turbulent flow field can affect the interaction strongly. Jamme (1998), Barre *et al.* (2000) and Mahesh, Lele & Moin (1997) have shown that the relative values of velocity fluctuations, temperature fluctuations, pressure fluctuations and velocity–temperature correlations play an important role in the amplification of velocity fluctuations across the shock and in affecting other aspects of the interaction. Higher values of velocity and vorticity amplifications have been observed when the sign of the correlation between velocity and temperature fluctuations is negative. The thermodynamic aspects of the incoming turbulence may change the effects of Mach number or Reynolds number by up to 100% in certain cases. An attempt has been mode here to characterize the thermodynamic state of the present flow field.

Table 3 provides values of the relative velocity and density fluctuations, $u_{rms}/\bar{U}_1$ and $\rho_{rms}/\bar{\rho}$, as well as the $R_{u\theta}$ correlation coefficient for the flow field before and after the interaction with the shock wave. Values of $R_{u\theta}$ in the upstream region are between −0.2 and −0.5. Under the strong Reynolds analogy (SRA) assumptions of Morkovin this value should be $R_{u\theta} = -1$. In the present work the assumption of negligible total temperature fluctuations, which is part of the SRA theory, was not invoked. In that respect it is not expected that the present correlations should be equal to −1.

The data of table 3 show that the relative velocity and density fluctuations are amplified through the interaction although mean values of velocity and density change through the interaction. There is also a decrease in $R_{u\theta}$ in the case of the finer grid 3×3 where scales are smaller than in the case of the 2×2 grid. In all cases, $R_{u\theta}$

		Before interaction			After interaction		
No.	Grid	$u_{rms}/\bar{U}_1$	$\rho_{rms}/\bar{\rho}$	$R_{u\theta}$	$u_{rms}/\bar{U}_1$	$\rho_{rms}/\bar{\rho}$	$R_{u\theta}$
1	2 × 2	0.029	0.0018	−0.5	0.066	0.0024	−0.54
2	2 × 2	0.0247	0.0024	−0.46	0.058	0.005	−0.6
3	3 × 3	0.0169	0.0031	−0.2	0.075	0.009	−0.32
4	3 × 3	0.013	0.0026	−0.3	0.0748	0.0098	−0.42

TABLE 3. Thermodynamic properties of flow before and after the interaction.

seems to increase after the interaction. The measured values of $R_{u\theta}$ in the downstream region appear to be in the range of −0.2 to −0.54 found by Mahesh *et al.* (1997) for interactions with shock wave strengths similar to the present ones.

The definitions of the mean and fluctuating Mach number can also be used to extract the contributions of the thermodynamic properties of the flow:

$$M = \bar{M} + M' = \frac{(\bar{U}+u)}{[\gamma R(\bar{T}+\theta)]^{1/2}} = \frac{(\bar{U}+u)}{[\gamma R\bar{T}(1+\theta/\bar{T})]^{1/2}} = \frac{(\bar{U}+u)}{[\gamma R\bar{T}]^{1/2}}\left[1 - \tfrac{1}{2}\frac{\vartheta}{\bar{T}} + \tfrac{3}{8}\frac{\vartheta^2}{\bar{T}^2} + \ldots\right].$$

After ignoring higher-order terms and averaging, this expansion leads to the following relation for the mean Mach number:

$$\bar{M} = \left[1 - \tfrac{1}{2}R_{u\vartheta}\left(\frac{u_{rms}}{\bar{U}}\right)\left(\frac{\vartheta_{rms}}{\bar{T}}\right) + \tfrac{3}{8}\frac{\overline{\vartheta^2}}{\bar{T}^2}\right]M_u \tag{8.1}$$

where M_u is the flow Mach number upstream of the shock. The fluctuating part after ignoring second-order and higher terms, appears to be:

$$M' = \left[\frac{u}{\bar{U}} - \tfrac{1}{2}\left(\frac{\vartheta}{\bar{T}}\right)\right]M_u.$$

The last equation can provide the variance of Mach number fluctuations as

$$\overline{M'^2} = \left[\frac{\overline{u^2}}{\bar{U}^2} - R_{u\vartheta}\left(\frac{\vartheta_{rms}}{\bar{T}}\right)\left(\frac{u_{rms}}{\bar{U}}\right) + \tfrac{1}{4}\frac{\overline{\vartheta^2}}{\bar{T}^2}\right]M_u^2.$$

or in terms of $M_t = u_{rms}/[\gamma R\bar{T}]^{1/2}$

$$\overline{M'^2} = \left[1 - R_{u\vartheta}\left(\frac{\vartheta_{rms}}{\bar{T}}\right)\Big/\left(\frac{u_{rms}}{\bar{U}}\right) + \tfrac{1}{4}\frac{\overline{\vartheta^2}}{\bar{T}^2}\Big/\frac{\overline{u^2}}{\bar{U}^2}\right]M_t^2. \tag{8.2}$$

The above relations reveal that the fluctuating Mach number does not only depend on the individual fluctuating velocity and thermal fields but also on their coupling through their correlation $R_{u\theta}$. The two terms which contain the correlation $R_{u\theta}$ in relations (8.1) and (8.2) in principle can change sign depending on the sign of $R_{u\theta}$. In the present cases all measured values of $R_{u\theta}$ are negative and therefore the final contribution of these terms is positive.

Each of the contributing terms appearing in both (8.1) and (8.2) has been computed from the experimental data obtained and the results are shown in table 4. The last two terms of (8.1) are of the order of 10^{-6} and consequently their contributions are extremely minimal. Therefore $\bar{M} = M_u$ is valid to a very good approximation. The two terms in the fluctuating Mach number relation (8.2) appear to be of the order of 10^{-2} and 10^{-3} with the term involving $R_{u\theta}$ being the most dominant. This results in values of the ratio M'_{rms}/M_t of between 1.015 and 1.034 in the upstream region and

No.	Grid	$-R_{u\theta}\left(\frac{\theta_{rms}}{\bar{T}}\right)\Big/\left(\frac{u_{rms}}{\bar{U}_1}\right)$ $(\times 10^3)$	$\frac{1}{4}\frac{\overline{\theta^2}}{\bar{T}^2}\Big/\frac{\overline{u^2}}{\bar{U}^2}$ $(\times 10^3)$	$\frac{M'_{rms}}{M_t}$	$-R_{u\theta}\left(\frac{\theta_{rms}}{\bar{T}}\right)\Big/\left(\frac{u_{rms}}{\bar{U}_1}\right)$ $(\times 10^3)$	$\frac{1}{4}\frac{\overline{\theta^2}}{\bar{T}^2}\Big/\frac{\overline{u^2}}{\bar{U}^2}$ $(\times 10^3)$	$\frac{M'_{rms}}{M_t}$
1	2×2	31	0.963	1.015	19.7	0.33	1.012
2	2×2	44	2.360	1.022	51	1.85	1.026
3	3×3	36	8.4	1.021	38.4	3.6	1.020
4	3×3	60	10	1.034	55.0	4.3	1.029

Table 4. Values of thermodynamic quantities appearing in Mach number relation of flow before and after the interaction.

slightly less in the downstream region. Thus these thermodynamic terms change M'_{rms} from 1.5% to 3.4%.

9. Vorticity and enstrophy in the flow field

A better understanding of the nature of the interaction of turbulent structures and vortex motions of turbulent flows with shock waves requires information on important quantities like vorticity, rate-of-strain tensor and its matrix invariants, and dissipation of turbulent kinetic energy. These flow quantities, although computationally as well as experimentally demanding, when resolved to proper scales are therefore well-suited for describing physical phenomena in vortical flows. One of the fundamental questions is how vorticity is transferred through shock waves. Ribner (1953) considered the case as a vorticity wave, which is transmitted through the shock according to Snell's law. In the present work, however, the transport equations of vorticity and enstrophy will be used to gain further insight into the processes involved in the interactions of shock waves with turbulence by looking at the instantaneous signals of the various quantities involved. The transport equation of vorticity

$$\frac{\mathrm{D}\Omega_i}{\mathrm{D}t} = S_{ik}\Omega_k - \Omega_i S_{kk} + \varepsilon_{iq\eta}\frac{1}{\rho^2}\frac{\partial \rho}{\partial x_q}\frac{\partial p}{\partial x_\eta} + \varepsilon_{iq\eta}\frac{\partial}{\partial x_q}\left(\frac{1}{\rho}\frac{\partial \tau_{\eta j}}{\partial x_j}\right) \qquad (9.1)$$

describes four dynamically significant processes for the vorticity component Ω_i, namely stretching or compression and tilting by the strain S_{ik}, vorticity generation through dilatation, baroclinic generation through the interaction of pressure and density gradients, and viscous effects expressed by the viscous stress term. The term $S_{ik}\Omega_k$ consists of one stretching or compression component and two tilting components. This term presumably plays an important role in the various processes involved which is not yet fully understood. The viscous term may also describe reconnection of vortex lines at very small scales due to viscosity. If the viscous term can be ignored since its magnitude, very often, is small, then the change of vorticity of a fluid element in a Lagrangian frame of reference can be entirely attributed to vortex stretching and/or tilting, to dilatational effects and to baroclinic torque.

If (9.1) is multiplied by Ω_i then the transport equation for the enstrophy $\frac{1}{2}\Omega_i\Omega_i$ can be obtained:

$$\frac{D\left(\frac{1}{2}\Omega_i\Omega_i\right)}{Dt} = S_{ik}\Omega_k\Omega_i - \Omega_i\Omega_i S_{kk} + \varepsilon_{iq\eta}\frac{1}{\rho^2}\Omega_i\frac{\partial \rho}{\partial x_q}\frac{\partial p}{\partial x_\eta} + \varepsilon_{iq\eta}\frac{\partial}{\partial x_q}\left(\Omega_i\frac{1}{\rho}\frac{\partial \tau_{\eta j}}{\partial x_j}\right) - \varepsilon_{iq\eta}\frac{1}{\rho}\frac{\partial \Omega_j}{\partial x_q}\frac{\partial \tau_{\eta j}}{\partial x_j}. \qquad (9.2)$$

The physical meaning of the terms associated with the time-dependant changes of enstrophy of a fluid element in a Lagrangian frame of reference are similar with those responsible for the generation or destruction of vorticity. The physical mechanisms involved in these complex processes are not fully understood. Enstrophy is a very significant quantity in fluid dynamics because it is not only related to the solenoidal dissipation, but also to several of the invariants of the strain-of-rate matrix S_{ij}, which may lead to detection of vortex tubes and shear layers in the flow field. In addition, enstrophy is a source term in the transport equation of dilatation S_{kk}:

$$\frac{\mathrm{D}S_{kk}}{\mathrm{D}t} = -S_{ik}S_{ki} + \tfrac{1}{2}\Omega_k\Omega_k + \frac{1}{\rho^2}\frac{\partial\rho}{\partial x_k}\frac{\partial p}{\partial x_k} - \frac{1}{\rho}\frac{\partial^2 p}{\partial x_k \partial x_k} + \frac{\partial}{\partial x_k}\left(\frac{1}{\rho}\frac{\partial \tau_{kq}}{\partial x_q}\right). \tag{9.3}$$

This transport equation describes the change of dilatation along a particle path which can be caused by the straining action of the dissipative motions ($S_{ik}S_{ik}$) as well as by the rotational energy of the spinning motions as it is expressed by the enstrophy $\frac{1}{2}\Omega_i\Omega_i$. Pressure and density gradients as well as viscous diffusion can also affect dilatation. It should be noted that the above transport equation reduces to the well-known Poisson equation for incompressible flows of constant density ($S_{kk} = 0$).

Figures 10(*a*) and 10(*b*) show signals of longitudinal velocity component U_1, lateral velocity component U_3, longitudinal and lateral vorticity components Ω_1 and Ω_2, dilatation $S_{kk} = (1/v)\mathrm{D}v/\mathrm{D}t = -(1/\rho)\mathrm{D}\rho/\mathrm{D}t$, dilatational dissipation $E_d = S_{kk}S_{kk}$, enstrophy $\Omega_i\Omega_i$ and various terms associated with the stretching of vortex lines. Each signal has been normalized by its r.m.s. value upstream of the interaction. As a result signals with relatively large fluctuations are reduced and signals with relatively small fluctuations are expanded. Thus all signals have been brought to about the same amplitude level. This normalization also helps to determine whether the signal of the particular quantity is amplified or not after the interaction by observation and comparison of the respective scale of fluctuations. The level of amplification is determined by the gain, G, which is defined in terms of a representative variable Q as the ratio $G_Q = Q_{rms,d}/Q_{rms,u}$ where the superscripts u and d denote regions upstream and downstream of the interaction respectively.

Each of the signals, with the exception of that of U_1, has been displaced by multiples of 10 r.m.s. units to allow better visibility. The shock wave location is evident on the longitudinal velocity signal where its value drops substantially. An inspection of the level of fluctuations after the passage of the shock and actual computation of their r.m.s. values indicates that some signals are amplified and some not. The longitudinal vorticity Ω_1 and lateral velocity U_3 signals are only slightly affected by the interaction. The computed data of this case show a 2% to 5% reduction in the r.m.s. values which indicates, within the experimental uncertainty, no significant changes in the transmission of Ω_1 and U_3 through the shock. Longitudinal velocity fluctuations and lateral vorticity fluctuations Ω_2 are substantially amplified through the interaction with gains of about 1.3. This characteristic is clearly demonstrated in figure 10(*c*) where the probability of appearance of lateral vorticity fluctuations upstream and downstream of the shock wave is plotted. These data show a substantially wider range of $\Omega_{2,d}$ fluctuations than that of $\Omega_{2,u}$.

Fluctuations of enstrophy $\Omega_k\Omega_k$ also show gains of the order of 1.1 to 1.5. Figure 11(*a*) shows the probability distributions of enstrophy fluctuations upstream and downstream of the shock regions for the case of the 2×2 grid with mesh size $M = 12.7$ mm. Data from experiments with two different shock strengths are plotted in this figure. The results of both experiments indicate higher enstrophy amplifications in the downstream regions. Similar behaviour is shown by the results obtained in the

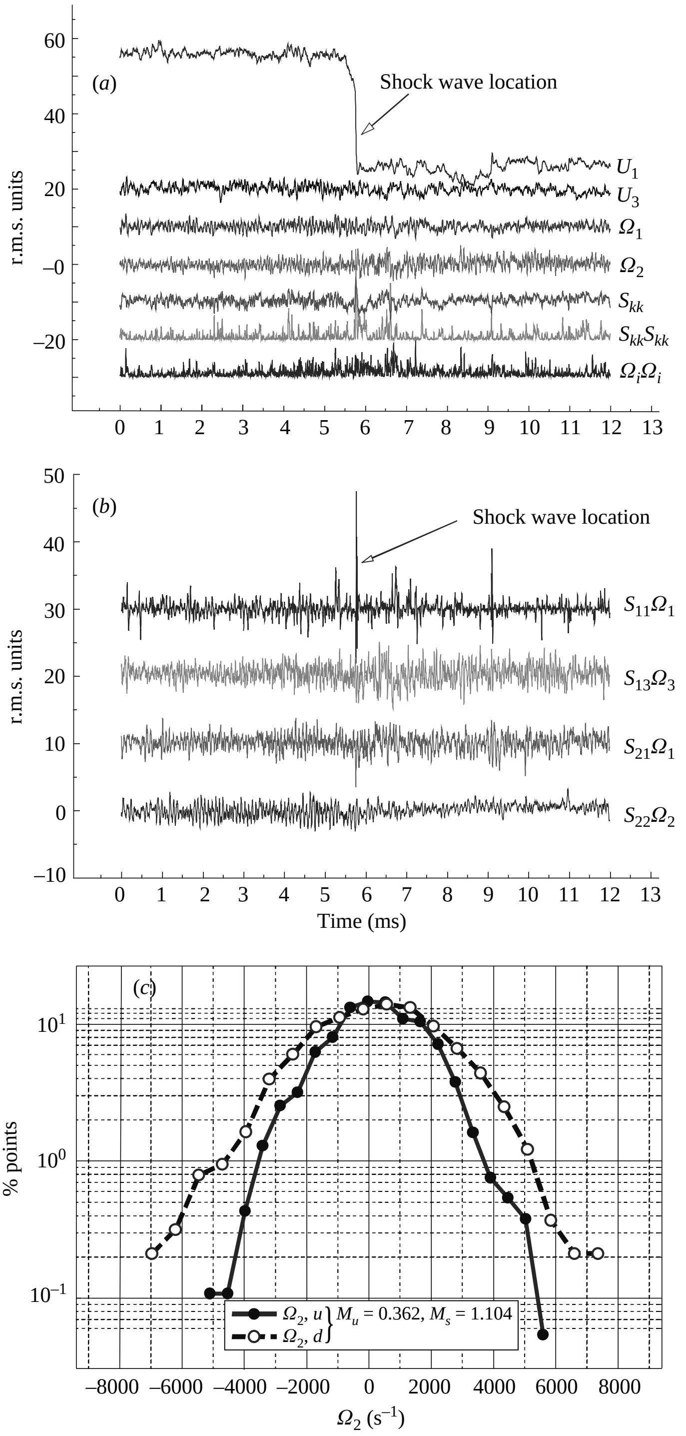

FIGURE 10. Time-dependent signals of (*a*) various quantities and (*b*) stretching/compression or tilting terms during an interaction with a shock wave of strength $M_s = 1.104$. (*c*) Probability plots of lateral vorticity fluctuations $\Omega_{2,u}$ and $\Omega_{2,d}$, upstream and downstream of the shock respectively.

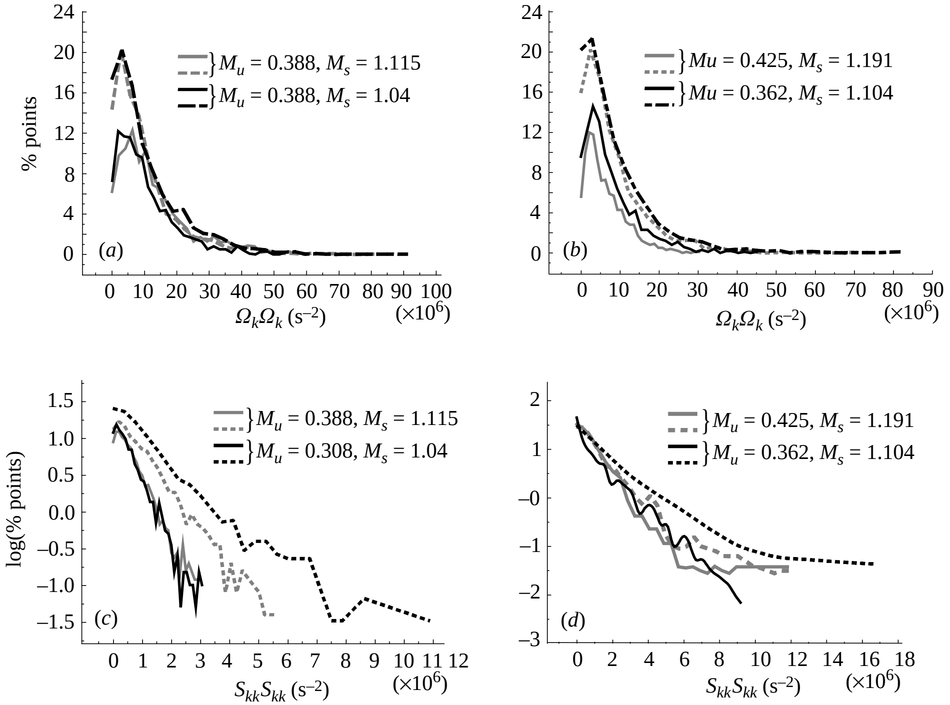

FIGURE 11. Probability plots of (*a*) enstrophy fluctuations $\Omega_k\Omega_k$, for the 2×2 grid, (*b*) enstrophy fluctuations $\Omega_k\Omega_k$, for the 3×3 grid, (*c*) dilatational dissipation fluctuations $S_{kk}S_{kk}$, for the 2×2 grid, (*d*) dilatational dissipation fluctuations $S_{kk}S_{kk}$, for the 3×3 grid. 2×2 grid: $M, = 12.7$ mm, 3×3 grid: $M = 8.5$. Solid lines, upstream; dashed lines, downstream.

experiments with the 3×3 grid with $M = 8.5$ mm, which are shown in figure 11(*b*). One common feature in the distributions of probabilities in all experiments shown in figures 11(*a*) and 11(*b*) is their long tails that suggests the existence of some rare events with large amplitude, which may play an important role in the processes of turbulent kinetic energy dissipation. The data show that the shock interaction starts to affect these high-amplitude events first. This is the first evidence that more high-amplitude events are present after the interaction.

Long tails in the probability distributions are also evident in the case of dilatational dissipation data $S_{kk}S_{kk}$, which are plotted in figures 11(*c*) and 11(*d*) for the 2×2 and 3×3 grids respectively. In the case of the 2×2 grid these data show a clear enhancement of $S_{kk}S_{kk}$ fluctuations downstream of the interaction in both experiments with different shock strengths. In the case of the 3×3 grid, the data in figure 11(*d*) also show an enhancement in the levels of $S_{kk}S_{kk}$ after the interaction.

A closer look at the enstrophy and dilatational dissipation signals displayed in figure 10(*a*) reveals a strong intermittent behaviour which is characterized by bursts of high-amplitude events, which sometimes reaches values of up to 8 r.m.s. units followed by less violent time periods. It should be mentioned that fluctuations of dilatation S_{kk} are very small in this experiment, only 10% of the fluctuations of vorticity. These values are typical in flows with low fluctuations of Mach number. Consequently baroclinic vorticity generation is negligible since pressure fluctuations are also small. Thus the only source of vorticity change, in addition to viscous diffusion, is through the stretching or compression and tilting term $S_{ik}\Omega_k$. Signals of various terms of

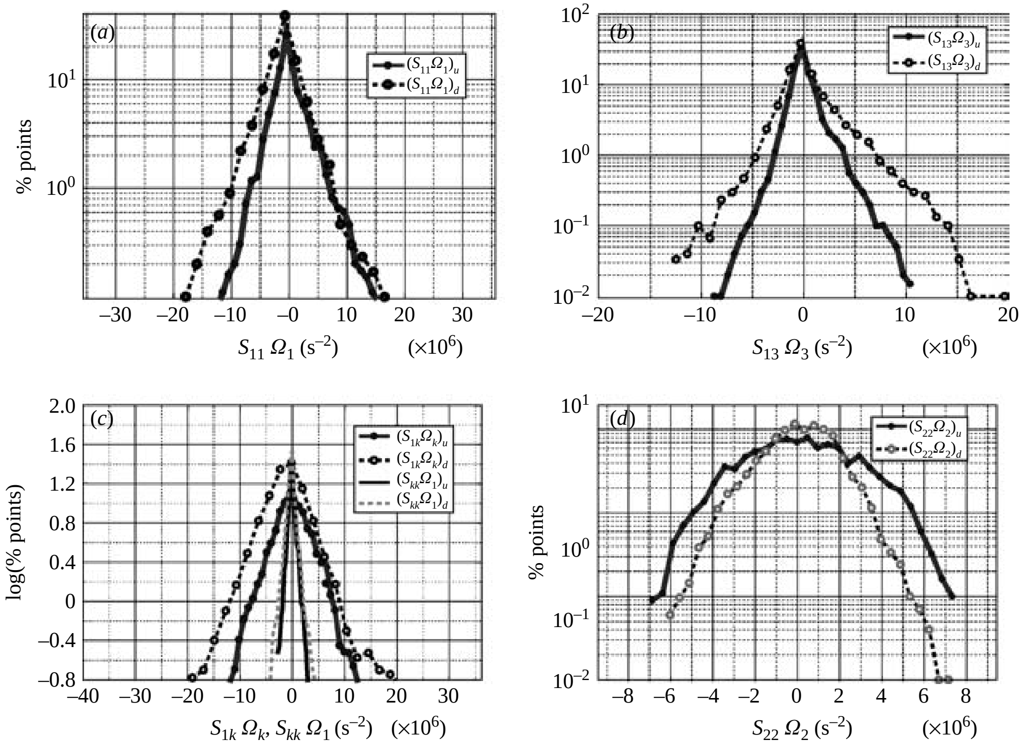

FIGURE 12. (*a*, *b*) Probability distributions of the stretching/compression term in the longitudinal direction, $S_{11}\Omega_1$ and $S_{13}\Omega_3$, before and after the interaction. (*c*) Probability distributions of the stretching/compression or tilting vector in the longitudinal direction, $S_{1k}\Omega_k$, and dilatational stretching/compression $S_{kk}\Omega_1$ before and after the interaction (*d*) Probability distributions of the stretching/compression term in the longitudinal direction, $S_{22}\Omega_2$, before and after the interaction. $M_u = 0.308$, $M_s = 1.04$, 2×2 grid with $M = 12.7$ mm.

this quantity have been displayed in figure 10(*b*). They are also characterized by an intermittent behaviour with periods of weak activity followed by bursts of strong activity. A further look into the components of this vector indicates that the level of fluctuations of the terms $S_{11}\Omega_1$, $S_{22}\Omega_2$ and $S_{33}\Omega_3$, which are the terms indicating vortex stretching or compression, changes substantially. Downstream of the interaction, the term $S_{11}\Omega_1$ increases while $S_{22}\Omega_2$ and $S_{33}\Omega_3$ decrease. As will be shown later in table 5 the first term increases because S_{11} increases substantially in the downstream region, although Ω_1 exhibits minor changes through the interaction. Figure 12(*a*) shows the probability distributions of $S_{11}\Omega_1$ before and after the interaction. Both distributions are characterized by long tails that are indicative of rare events of important dynamic significance. The range and distribution of the fluctuations are larger in the downstream region than upstream. It should be mentioned here that the time-average values of all velocity gradients and therefore of S_{ij} and Ω_k practically vanish everywhere in the present flow except within the shock wave where several of the gradients, particularly in the longitudinal direction, reach values different from zero. In that respect, compression of vortex lines in the time-average sense is expected to take place only within the shock wave where $\overline{S_{11}\Omega_1}$ is expected to be non-zero. One of the most interesting features of vorticity as a quantity describing a flow field is that the level of fluctuations is large and very often an order of magnitude larger than its time-average values even in flows which are highly inhomogeneous (see Andreopoulos & Honkan 2001). In the present case, the r.m.s. level of $S_{11}\Omega_1$ fluctuations increases in the downstream region although its time-average is zero. A substantially larger increase in the r.m.s. values has been observed in the case of $S_{12}\Omega_2$ and $S_{13}\Omega_3$, which are part of the source/sink term indicating tilting of vortex lines. Figure 12(*b*) shows the probability distributions of the fluctuations of $S_{13}\Omega_3$ before and after the interaction. Long tails are also evident here. The probability distributions of the resultant component of the stretching vector in the longitudinal direction $S_{1k}\Omega_k = S_{11}\Omega_1 + S_{12}\Omega_2 + S_{13}\Omega_3$ before and after the interaction are shown in figure 12(*c*). It appears that the level of these fluctuations increases after the interaction. The source/sink terms in the transport equation of vorticity (9.1) contain contributions from the dilatation term $S_{kk}\Omega_i$. Probability distributions of the fluctuations of $S_{kk}\Omega_1$ are also shown in figure 12(*c*). They are substantially lower than the corresponding values of $S_{1k}\Omega_k$ and they increase after the interaction.

A notably different behaviour than that described above has been observed in the level of fluctuations of the stretching/compression term in the lateral directions x_2 and x_3. These fluctuations decrease after the interaction. This is evident in the probability distributions of $S_{22}\Omega_2$ shown in figure 12(*d*). The measured r.m.s. indicated a reduction of about 30%.

Clearly, compression by the shock wave reduces the level of vorticity fluctuations associated with the so-called mechanism of vortex line compression in the lateral direction and increases it in the longitudinal direction. Tilting of vorticity components by the action of the shear S_{ik} increases through the interaction by various amounts on each of the three vorticity components so as to compensate for the deficit caused by the vortex line compression. Thus the complete stretching term increases after the shock.

10. Dissipation rate of turbulent kinetic energy

The instantaneous dissipation rate of turbulent kinetic energy $q^2 = \frac{1}{2}U_iU_i$ converted into thermal/internal energy is given by

$$E = \tau_{ij}S_{ij} = 2\mu S_{ij}S_{ij} - \frac{2}{3}\mu\frac{\partial U_k}{\partial x_k}\frac{\partial U_m}{\partial x_m}. \tag{10.1}$$

It appears in the transport equation of q^2as a sink term and as a source term with positive sign in the transport equation for internal energy and entropy. The second term on the right-hand side of (10.1) represents the additional contribution of compressibility to the dissipation rate of kinetic energy. This term disappears in the cases of incompressible flows. Since this term is always positive, the negative sign in front may erroneously suggest that compressibility reduces dissipation. This is incorrect because the term $S_{ij}S_{ij}$ also contains contributions from dilatation effects, which can be revealed if one considers that

$$S_{ij}S_{ij} = \tfrac{1}{2}\Omega_k\Omega_k + \frac{\partial U_i}{\partial x_j}\frac{\partial U_j}{\partial x_i}. \tag{10.2}$$

The second term on the right-hand side represents the inhomogeneous contribution in the case of incompressible flows. In the case of compressible flows, terms related to dilatation can be extracted, and the instantaneous total dissipation rate then becomes

$$E = \mu\Omega_k\Omega_k + 2\mu\left[\frac{\partial U_i}{\partial x_j}\frac{\partial U_j}{\partial x_i} - S_{kk}S_{kk}\right] + \tfrac{4}{3}\mu S_{kk}S_{kk}. \tag{10.3}$$

The third term on the right-hand side describes the direct effects of compressibility, i.e. dilatation, on the dissipation rate. The first and the last terms on the right-hand side of (10.3) are quadratic with positive coefficients and positive signs and they are, therefore, always positive. The second term on the right-hand side indicates the contributions to the dissipation rate by the purely non-homogeneous part of the flow. Its time-averaged contribution disappears in homogeneous flows. This term, in principle, can attain negative values and thus it can reduce the dissipation rate. This does not violate the second thermodynamic law as long as the total dissipation remains positive at any point in space and time.

E can be decomposed into a solenoidal part E_s, which is the traditional incompressible dissipation, and a dilatational part E_d. In this case $E = E_s + E_d$ with

$$E_s = \mu \Omega_k \Omega_k + 2\mu \left[\frac{\partial U_i}{\partial x_j} \frac{\partial U_j}{\partial x_i} - S_{kk} S_{kk} \right]$$

and $E_d = 4/3 \mu S_{kk} S_{kk}$. We can further define for convenience

$$E_R = \mu \Omega_k \Omega_k, \quad E_h = 2\mu \left[\frac{\partial U_i}{\partial x_j} \frac{\partial U_j}{\partial x_i} - S_{kk} S_{kk} \right] \text{ and } E_q = \frac{\partial U_i}{\partial x_j} \frac{\partial U_j}{\partial x_i}.$$

Figure 13(*a*) contains signals of the various components of the total dissipation E discussed above with values divided by μ. All the components have positive values at all times with the exception of the inhomogeneous part

$$\frac{E_h}{2\mu} = \left[\frac{\partial U_i}{\partial x_j} \frac{\partial U_j}{\partial x_i} - S_{kk} S_{kk} \right],$$

which alternates between positive and negative values. Its time-average is zero, as expected in this isotropic flow, but instantaneously it can reach values that are non-negligible. In that respect it can reduce the value of the solenoidal dissipation, E_s and therefore reduce E, which, however, never becomes negative. The fact that the present data indicate always positive values of E provides some reliability in the quality of the measurements and allows confidence in further using these data.

The relation between enstrophy and dissipation rate is of great interest. Figure 13(*b*) shows a scatter plot of enstrophy and dissipation rate data upstream and downstream of the interaction. The density of the scattered data points is equivalent to the joint probability between these quantities. The most probable values are located close to the point $(5 \times 10^6, 6 \times 10^6)$ upstream of the interaction region. However, of interest are events with large values of either or both of these quantities, which although having low probability of appearance are indicative of significant dynamical processes. Large values of enstrophy and dissipation rate may be associated with the existence of local shearing. Events with low values of enstrophy and large values of dissipation rate are indicative of irrotational dissipation, while events with high values of enstrophy and low values of dissipation rate are indicative of the existence of vortex tubes in the flow.

The data of figure 13(*b*) indicate that dissipation dominates the flow motions more than enstrophy. This is evident if one compares values of dissipation and enstrophy at locations of about the same point density. The present data show some weak activity of non-dissipative vortex tubes while substantial irrotational dissipative motions can be observed. Downstream of the interaction, the ranges of both quantities increase. Events indicative of non-dissipative vortex tubes and irrotational dissipative motions are more intense in this region than upstream of the shock. There is also a significant

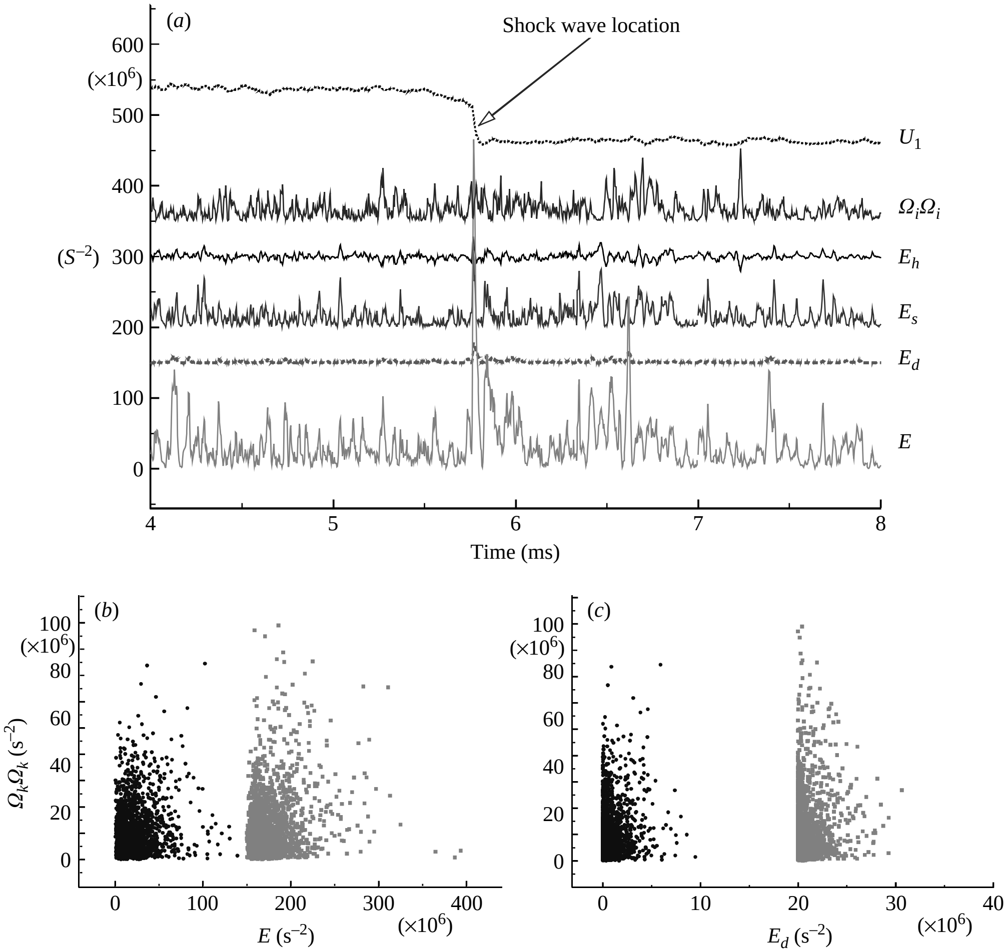

FIGURE 13. (*a*) Signals of total dissipation, E/μ; solenoidal dissipation, E_s/μ; dilatational dissipation, E_d/μ; inhomogeneous contribution, $E_h/2\mu = [(\partial U_i/\partial x_j)(\partial U_j/\partial x_i) - S_{kk}S_{kk}]$ and enstrophy. Signals are displaced by 0, 150, 200, 300 and 350 s^{-2} units respectively. Velocity U_1 signal is in $\mathrm{m\,s}^{-1}$ and it displaced by 400 s^{-2} units. (*b, c*) Scatter plots of enstrophy, $\Omega_k\Omega_k$ and dissipation, E/μ data in (*b*) and E_d/μ in (*c*), upstream and downstream of the interaction with a shock wave of $M_s = 1.104$. Downstream data have been displaced by 150 units in (*b*) and 20 units in (*c*).

increase in the number of events with intense rotational and dissipative motions, which suggest the existence of isolated vortices or shear layers.

Scatter plots of enstrophy and dilatational dissipation data upstream and downstream of the interaction are shown in figure 13(*c*). Compressibility effects are not strong in the present flows. Rotational activities dominate the flow processes over dilatational effects. Most of these strong activities are associated with small but not negligible dilatational dissipation.

As was demonstrated in figure 13(*a*) the inhomogeneous part of the solenoidal dissipation, E_h, is not negligible during these dynamically significant processes although its time-averaged effect is zero. Large-amplitude fluctuations, for instance, may be associated with the passage of individual vortices or strong shear layers, which could also be associated with high-enstrophy and high-dissipation events. Figure 14(*a*)

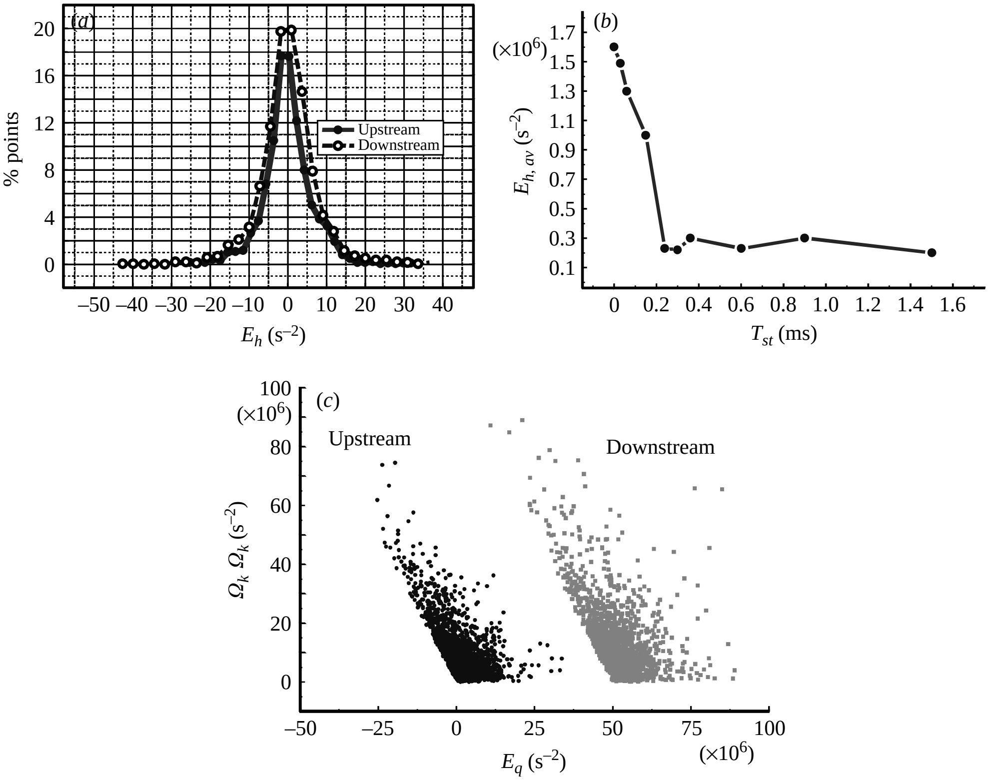

FIGURE 14. (*a*) Probability distributions of homogeneous dissipation E_h/μ upstream and downstream of the interaction with a shock wave of $M_s = 1.104$. (*b*) Return-to-isotropy data downstream of the interaction with a shock wave $M_s = 1.104$. Homogeneous dissipation E_h/μ vs. starting time of integration. (*c*) Scatter plot of enstrophy and E_q data, upstream and downstream of the interaction. Values downstream of interaction are displaced by 50 units.

shows the probability distribution of E_h values before and after the interaction. The distribution of data of the downstream region is characterized by larger-amplitude fluctuations and higher probabilities than the upstream data. This behaviour may suggest that the flow downstream of the interaction may be substantially less isotropic than the upstream flow. The time-averaged value of E_h is rather small in comparison to the other components of dissipation. The fact, however, that the shock wave which is causing the interaction is an axisymmetric disturbance and that the incoming flow is isotropic suggests that the outcome flow is non-isotropic. On the other hand, there is a tendency to return to isotropy by the action of pressure fluctuations. In order to find out when the return to isotropy takes place, the quantity E_h has been used as an indicator and its time-average value

$$E_{h,av} = \frac{1}{T}\int_{T_{st}}^{T_e} E_h(t)\,\mathrm{d}t$$

has been computed for various values of T_{st}, which is the time of starting the integration. Most of the events contributing to anisotropy are expected to be present immediately after the passage of the shock wave and therefore the return to isotropy can be determined by fixing the upper limit of the integration, T_e, and varying the lower limit T_{st}. The results are shown in figure 14(*b*). Ideally, $E_{h,av}$ should be zero in a perfectly isotropic flow. In the present case, $E_{h,av}$ decreases fast when the shifting of T_{st} starts and after about 0.2 ms reaches a level with a constant value of about $0.23 \times 10^6\,\mathrm{s}^{-2}$. It is therefore believed that the return to isotropy process has been completed within 0.2 ms. This time is considered reasonably short and it represents a rather small fraction of the duration of useful data downstream of the shock wave. In that respect, the reduced integration time/number of samples has no impact on the statistical averages.

Finally the quantity $-S_{ik}S_{ki} + \frac{1}{2}\Omega_k\Omega_k$ is of interest because it is one of the source/sink terms appearing in the transport equation of S_{kk} (9.3). It is related to E_q as

$$E_q = \frac{\partial U_i}{\partial x_j}\frac{\partial U_j}{\partial x_i} = S_{ij}S_{ij} - \tfrac{1}{2}\Omega_k\Omega_k.$$

Since it has been argued that baroclinic effects before and after the interaction are negligible, E_q and the pressure hessian term, $-(1/\rho)(\partial^2 p/\partial x_k \partial x_k)$, are controlling the change in dilatation along a particle path if viscous effects are also negligible. The term itself indicates whether straining or rotational activities dominate the dynamical processes. The relation of E_q to enstrophy has been further explored by considering their scatter plot data shown in figure 14(*c*) for the regions upstream and downstream of the shock. Two lines with slopes $-1/2$ and 0 bound the data plotted in this figure. Positive values of E_q suggest that flow-straining activities dominate the local processes more than rotation. The time-average value of E_q is small but its instantaneous fluctuations can burst to about 30 times larger values.

The region upstream of the shock is characterized by events of high positive E_q and low rotational activities where straining is dominant and by events of large negative E_q values and high enstrophy. Events of large values of both E_q and enstrophy are rather scarce. On the contrary, events with high positive E_q and high E_R are plentiful downstream of the interaction region. Straining activities are more dominant in these cases.

In general, if the contributions of the pressure hessian term are not considered, positive E_q is expected to cause a decrease in S_{kk} and therefore a decrease in the specific volume, i.e. compression, since $S_{kk} = (1/v)\,\mathrm{D}v/\mathrm{D}t$. If E_q is negative, i.e. events with high rotational activities are dominant, then flow expansion may take place temporarily.

The alignment between the velocity and vorticity vectors and its relation to the dissipation rate is of interest. Helicity is defined as the scalar product between the velocity and vorticity vectors, $h = \boldsymbol{U} \cdot \boldsymbol{\Omega} = |\boldsymbol{U}|\,|\boldsymbol{\Omega}| \cos\theta_h$ where θ_h is the angle between the two vectors $\boldsymbol{U}$ and $\boldsymbol{\Omega}$. According to Moffatt (1969) the volume integral of h is invariant under certain flow conditions. The mean value of h is evidently zero if the isotropic turbulence possesses the reflectional symmetry property. In a purely solenoidal flow this vector product should be zero since the two vectors are always orthogonal. Figure 15(*a*) shows probability distributions of helicity obtained from the time-dependent data of two different experiments with the 2×2 grid. The distributions are quite narrow and spiky with long tails and with mean and most probable values very close to zero. The range appears to be wider in the downstream region indicating higher fluctuations of helicity. Thus mean helicity is not affected by the interaction with the shock while its r.m.s. value increases after the interaction.

Values of $\cos\theta_h$ have been computed and their probability distributions are shown in figure 15(*b*). The distribution is flat within 1% in the range $-0.9 < \cos\theta_h < 0.9$ which corresponds to $25^\circ < \theta_h < 155^\circ$ and it increases beyond this range suggesting that the two vectors tend to be parallel. The distributions upstream of the shock

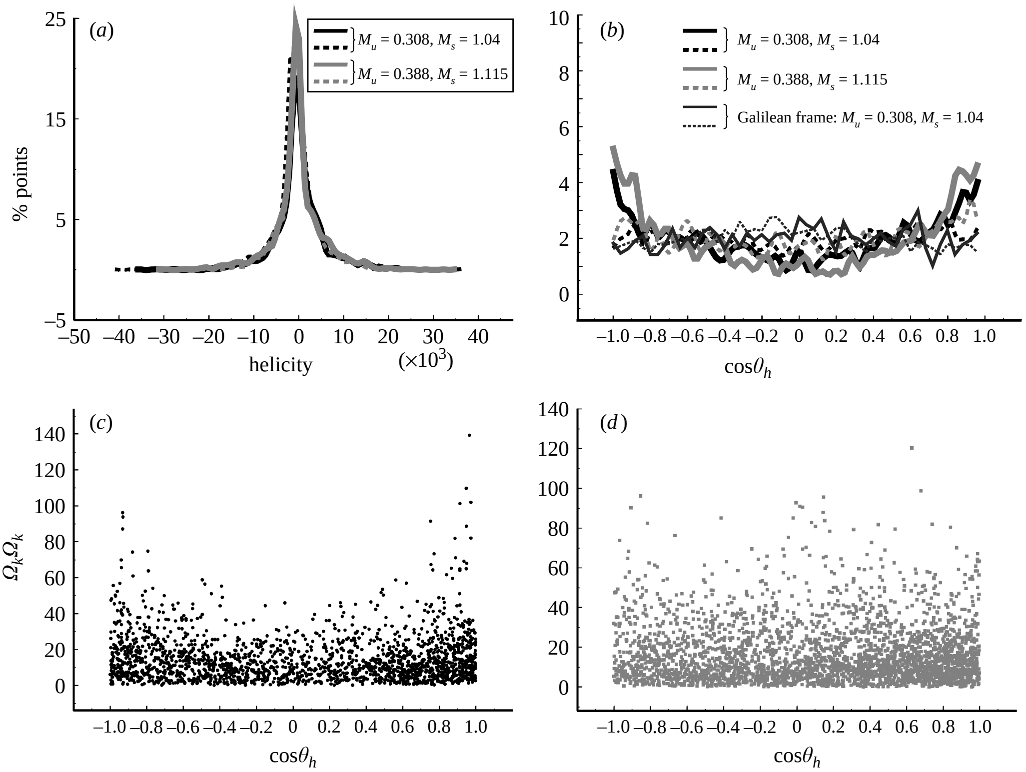

FIGURE 15. (*a*) Probability distributions of helicity in various interactions with the 2×2 grid. (*b*) Probability plots of alignment angle between velocity and vorticity vectors in the case of the 2×2 grid with $M = 12.7$ mm. Solid lines, upstream values; dotted lines, downstream values. (*c, d*) Scatter plots of enstrophy or rotational dissipation $E_R/\mu = \Omega_k\Omega_k$ and helicity density (*c*) upstream and (*d*) downstream of the interaction, in the case of the 2×2 grid with $M_u = 0.308$ and $M_s = 1.04$.

wave region show no asymmetry and their average appears to be close to $\theta_h \approx 90°$. However the upward trend near the edges of the distribution is indicative of a minor lack of reflectional symmetry that has been also observed in low-speed isotropic flows (see Tsinober, Kit & Dracos 1992). This may be due to the fact that $\cos\theta_h$ is not a Galilean invariant because it involves the total velocity vector in the computations. In a purely isotropic turbulence, $\cos\theta_h$ is Galilean invariant. Probability distributions of $\cos\theta_h$ for an observer moving with the mean flow on a Galilean-invariant frame are also shown in figure 15(*b*). Distributions both before and after the interaction appear to be reasonably constant with values falling towards the edges. Thus, there is no preferential alignment between velocity and vorticity fluctuations, a conclusion in agreement with the work of Wallace, Balint & Ong (1992).

The lack of constant probability distribution may be interpreted by considering the classical decomposition of the velocity field into a solenoidal contribution and a potential part. The lack of symmetry in the measured distribution may indicate a large influence of the potential part while in highly vortical regions the solenoidal contribution dominates over the potential part, reducing the degree of asymmetry. A closer look into the time-dependent signals of the three components of helicity $U_i\Omega_i$ indicated that during events with high or low values of one of the two quantities U_i or Ω_i, the other one crosses the zero level resulting in values of helicity very close to zero.

Downstream of the interaction the trend of the preferential orientation between $\boldsymbol{U}$ and $\boldsymbol{\Omega}$ vanishes and the probability distributions are more evenly distributed across all angles.

The relation between the rotational dissipation rate $E_R = \mu\Omega_k\Omega_k$ and helicity h can be depicted by considering the scatter plots between h and E_R/μ shown in figures 15(c) and 15(d). It appears that weak or moderate rotational dissipation rate E_R/μ is evenly distributed across all orientation angles before the interaction. Events with high values of dissipation rate occur when the orientation between vorticity and velocity is 0° and 180°. In the region downstream of the interaction, however, dissipation with moderate or low values appears to take place during all orientations with some weak preference towards the 0° value. Significantly more events at high dissipation rates were observed occurring at various angles or bands of alignment angles about 45°, 90° and 155°.

The dynamically important alignment between the vorticity vector $\boldsymbol{\Omega}$ and its stretching vector $\boldsymbol{W}$ with components $W_1 = S_{1k}\Omega_k$, $W_2 = S_{2k}\Omega_k$ and $W_3 = S_{3k}\Omega_k$, is also of interest. If φ_s is the angle between $\boldsymbol{\Omega}$ and $\boldsymbol{W}$ then $\cos\varphi_s = \boldsymbol{\Omega}\cdot\boldsymbol{W}/|\boldsymbol{\Omega}|\,|\boldsymbol{W}|$. The scalar product $\boldsymbol{\Omega}\cdot\boldsymbol{W}$ is of particular importance because $\boldsymbol{\Omega}\cdot\boldsymbol{W} = \Omega_i S_{ik}\Omega_k$ is the source term in the transport-of-enstrophy equation (9.2). If this equation is time-averaged then this term is the most dominant among the terms appearing in the resultant equation since it is cubic in the velocity derivatives that are substantial in small scales. The advective term is usually small and in the case of incompressible flow this term counterbalances the viscous destruction term directly, which is always positive. In that respect and in the time-average sense this term should be always positive, and therefore it can be concluded that vortex stretching or tilting always amplifies enstrophy of small-scale turbulence. Batchelor & Townsend (1947) linked this quantity to the skewness of the velocity derivative $\partial U_1/\partial x_1$. The importance of the positiveness of this term is somewhat overstated (see for instance Tsinober *et al.* 1992) because it is a result of time-averaging the transport equation that completely masks the dynamically significant processes involved. The r.m.s. value of this quantity is much larger than its mean. Positive or negative excursions of this term with amplitude up to 300 times its mean are common (see Andreopoulos & Honkan 2001). Thus negative values suggesting simply a reduction in enstrophy are not in violation of any physical law. In addition, the assumptions involved in deriving this argument ignored completely the advection term and the coupling between mean flow and turbulence. This would be justified only in extremely high-Reynolds-number isotropic turbulent flow.

Typical probability distributions of the term $\Omega_i S_{ik}\Omega_k$ are shown in figure 16(a) for only one experiment. The distributions are narrow with long tails. In the upstream region the range is between -2.5×10^5 and 2.0×10^5 with mean at $1500\,\mathrm{s}^{-3}$. Downstream of the interaction region the mean value is about $750\,\mathrm{s}^{-3}$, while the range and therefore the level of fluctuations increased by 60%.

Probability plots of $\cos\varphi_s$ are shown in figure 16(b) for two different interactions with the 2×2 grid. In almost all the cases the most probable values of $\cos\varphi_s$ are close to the edges of the distributions, suggesting that the two vectors tend to be parallel to each other and in the same or opposite directions. The not unusual lack of symmetry found in the experiments of Tsinober *et al.* (1992) is also found here. This, however, is a genuine feature of the distribution because it is related to a non-zero average value of $\Omega_i S_{ik}\Omega_k$ and it cannot be attributed to breakdown of symmetry.

The scatter plots between the dissipation rate E_R and $\cos\varphi_s$ shown in figure 16(c) indicate that E_R is evenly distributed across all orientation angles during events with low values of E_R. Vorticity and stretching vectors are parallel and in the same

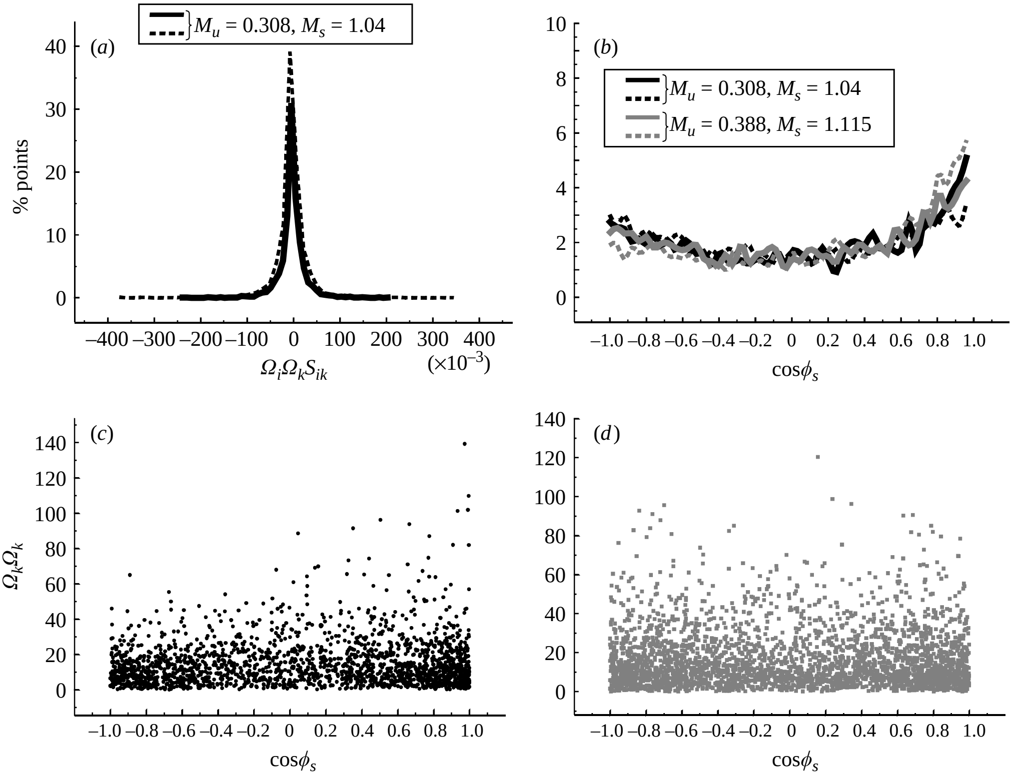

FIGURE 16. (*a*) Probability distribution of the enstrophy generation term $\Omega_i\Omega_k S_{ik}$ upstream and downstream of the interaction with the 2×2 grid. (*b*) Probability plots of alignment between vorticity and its stretching vector in the case of the 2×2 grid with $M = 12.7$ mm. Solid lines, upstream values; dotted lines, downstream values. (*c*, *d*) Scatter plots of enstrophy or rotational dissipation $E_R/\mu = \Omega_k\Omega_k$ and $\cos\varphi_s$ of the relative orientation between vorticity and stretching vectors (*c*) upstream and (*d*) downstream of the interaction in the case of the 2×2 grid with $M_u = 0.308$ and $M_s = 1.04$.

direction during events with substantial dissipation rate of kinetic energy. In the downstream region (see figure 16*d*) high and low values of dissipation are almost evenly distributed across the entire range of angle alignment. Low values of E_R, however, occur more when the two vectors are in the same or opposite directions.

The orientation between the vorticity vector $\boldsymbol{\Omega}$ and its dilatational stretching vector $\boldsymbol{W}_d$ with components $W_{d,1} = -S_{kk}\Omega_1$, $W_{d,2} = -S_{kk}\Omega_2$ and $W_{d,3} = -S_{kk}\Omega_3$, can be expressed as $\cos\varphi_d = \boldsymbol{\Omega} \cdot \boldsymbol{W}_d/|\boldsymbol{\Omega}|\,|\boldsymbol{W}_d|$. This scalar product is also of significance because it is the source term $-\Omega_i\Omega_i S_{kk}$ in (9.2). It appears that $\cos\varphi_d = -1$, which indicates that the two vectors are always in the opposite direction.

11. Turbulence length scales

One of the unresolved issues related to the present flow case is the behaviour of length scales downstream of the interaction. There is some disagreement between experimental results and DNS data on how the various length scales of turbulence are affected by the interaction with the shock wave. The DNS data of Lee *et al.* (1993) and Hannappel & Friedrich (1995) indicate that all characteristic length scales, namely longitudinal and lateral velocity integral length scales, longitudinal velocity

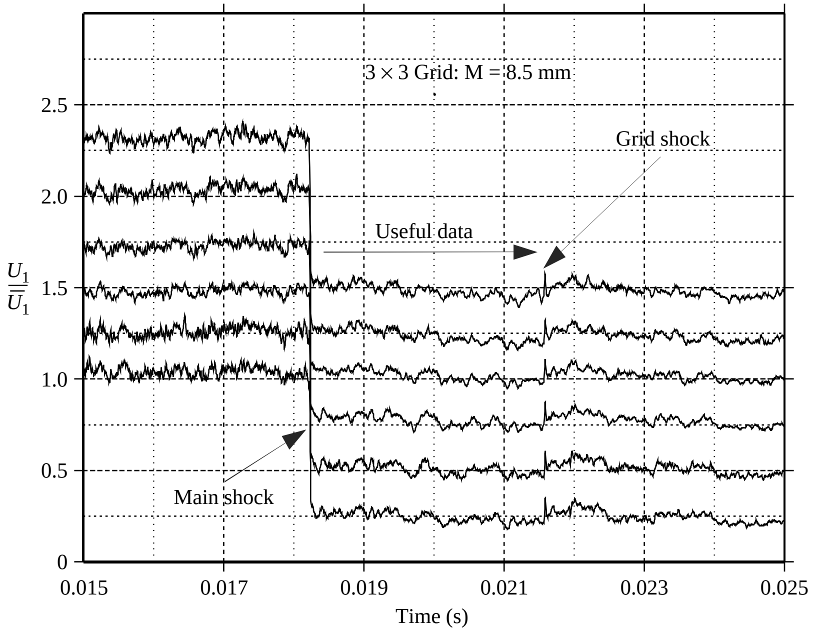

FIGURE 17. Time-dependent longitudinal velocity signals obtained with the hot-wire rake. Signals are displaced by multiples of 0.25 from each other. $M_u = 0.564$, $M_s = 1.39$.

microscale, dissipation length scale, as well as integral length scale and microscale of density fluctuations, decrease through shock interactions. The experimental data of Keller & Merzkirch (1990) show that the density microscale increases across the shock. Hannappel & Friedrich (1995) also show that the reduction in the Taylor's microscales parallel to the shock front is weaker by a factor of 2 when the compressibility level of the incoming turbulence is high. On the other hand, the dissipation length scale in the experiment of Honkan & Andreopoulos (1992) was also found to increase after the interaction. DNS results of Lee *et al.* (1994) have indicated a small increase of dissipative length scales through weak shock interactions. Thus, there is no agreement among various researchers on how shock interactions affect the length scales. Intuitively, one would expect that compression should reduce length scales.

In an effort to resolve the disagreement between experiments and DNS, detailed space–time correlation measurements were carried out by using a rake of six parallel wires and three temperature wires separated from each other by $\Delta\xi_2 = 1$ mm. In order to estimate the integral length scales in the longitudinal ξ_1 direction and normal ξ_2 direction values of the cross-correlation coefficient

$$r_{ij}(x, \xi_k) = \overline{u_i(x)u_j(x+\xi_k)} \Big/ \left(\overline{u_i^2(x)}\right)^{1/2} \left(\overline{u_j^2(x+\xi_k)}\right)^{1/2}$$

were obtained by two-point measurements in the ξ_2 direction and from auto-correlations after invoking Taylor's hypothesis in the ξ_1 direction. Thus with $\overline{U}_1 = \xi_1 \tau$ it appears that

$$L_{11}(x_1) = \int_0^\infty r_{11}(x_1, \xi_1)\,\mathrm{d}\xi_1 = \overline{U}_1 \int_0^\infty r_{11}(x_1, \tau)\,\mathrm{d}\tau.$$

Typical signals obtained with the hot-wire rake are shown in figure 17 for one shock interaction with turbulence produced by the 3×3 grid with mesh size $M = 8.5$ mm.

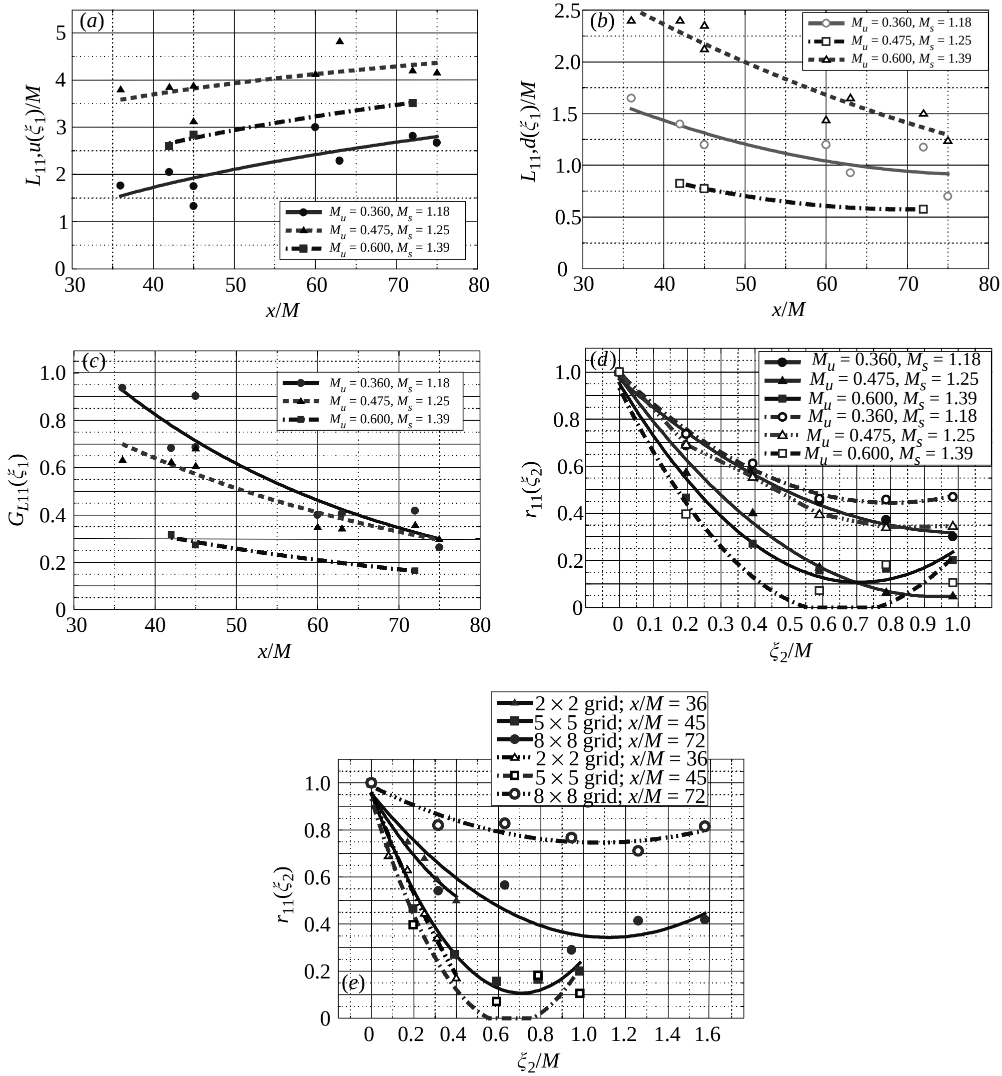

FIGURE 18. (*a*, *b*) Longitudinal integral length scales along the flow field (*a*) upstream and (*b*) downstream of the shock wave at different strengths of the interaction. (*c*) Ratio of the longitudinal integral length scale $G_{L11} = L_{11,d}(\xi_i)/L_{11,u}(\xi_1)$ for various strengths of the interaction. (*d*) Spatial correlations in the lateral direction for various strengths of the interaction. Data obtained at $x/M = 45$ with the 5×5 grid with $M = 5.1$ mm. (*e*) Spatial correlations in the lateral direction for the case of the interaction with $M_u = 0.6$ and $M_s = 1.39$. Data obtained at different locations with three different grids. Filled symbols, upstream of the interaction; open symbols, downstream of the interaction. in (*d*) and (*e*).

All values of the signals have been non-dimensionalized by the mean velocity in the longitudinal direction upstream of the interaction. The six signals appear reasonably correlated with each other. Cross- and auto-correlation functions were estimated from the time-dependent data for various cases. Integration of the correlation function was carried out numerically. The results are shown in figures 18(*a*) and 18(*b*) where data of the longitudinal integral length scale L_{11} are plotted for upstream and downstream of the interaction regions respectively. There exists some scatter in the data in each particular case, which is attributed to the various grids used. No attempt has been made to extract any Re_M effects since no clear trend or pattern among the data obtained could be identified. From the data of figure 18(*a*), it can be seen that the integral length scale $L_{11,u}(\xi_1)$ increases with downstream non-dimensional distance x/M for all investigated cases *before* the interaction. It is also evident that $L_{11,u}(\xi_1)$ in the case $M_u = 0.475$ is higher than in the case $M_u = 0.36$. However when the flow Mach number increases to $M_u = 0.6$ and therefore stronger compressibility effects are present, then the values of the integral length scale drop.

Downstream of the interaction with the shock wave the distribution of $L_{11,d}(\xi_1)$ is more complicated. All the scales decrease with x/M and they are reduced considerably from their upstream values. However the reduction of the larger scales is greater. This is better shown in figure 18(*c*) where the attenuation ratio $G_{L11} = L_{11,d}(\xi_1)/L_{11,u}(\xi_1)$ is plotted against x/M. At large x/M where the initial scales were the largest the reduction is dramatic. Thus once again it is found that amplification or attenuation is not the same for all initial length and velocity scales. It is interesting to observe that the stronger the shock strength the greater the attenuation of the longitudinal length scales. In this case, for instance, L_{11} is reduced by 70% to 85% from its upstream value.

The two-point correlation $r_{11}(\xi_2)$ of the longitudinal velocity fluctuations in the lateral direction ξ_2 is shown in figure 18(*d*). Because of the fixed separation between the six hot wires not all the curves cross the zero line and therefore it is very difficult to integrate them in order to obtain the classically defined length scale in the lateral direction. However the slopes of these curves are indicative of their trend. It is rather obvious that the length scales before interaction are reduced with increasing flow Mach number. This behaviour is very similar to that of $L_{11}(\xi_1)$. After the interaction, however, the length scale $L_{11}(\xi_2)$ increases in the first two cases and decreases in the strongest interaction.

In order to investigate the effect of initial conditions on this correlation at the highest flow and shock Mach number where the lateral scales are shown to reduce, experiments with various grids were carried out. The data obtained shown in figure 18(*e*) indicate that the correlation increases substantially in the case of the finest grid, 8 × 8 with the lowest Re_λ, after the interaction for the range of length scales investigated. However the coarser grid, the 2 × 2 grid with the highest $Re_\lambda = 737$, shows the greatest attenuation in the lateral integral scale of turbulence after the interaction.

Thus, integral length scales in the longitudinal direction were reduced after the interaction in all investigated flow cases. The corresponding length scales in the normal direction increase at low Mach numbers and decrease during stronger interactions. It appears that in the weakest of the present interactions, turbulent eddies are compressed in the longitudinal direction drastically while their extent in the normal direction remains relatively the same. As the shock strength increases the lateral length scale increases while the longitudinal decreases. At the strongest interaction of the present cases, the eddies are compressed in both directions. However, even at the highest Mach number the issue is more complicated since amplification of the lateral scales has been observed in fine grids. Thus the outcome of the interaction strongly depends on the initial conditions.

The curvature of the cross correlation function r_{ij} at the origin defines the Taylor microscale λ_{ik} through the relation

$$\left[\frac{\partial^2 r_{ii}}{\partial \xi_k^2}\right]_{\xi_k \to 0} = -\frac{1}{\lambda_{ik}}.$$

Although the number of data points in the vicinity of the origin is not adequate for an accurate determination of the second derivative of $r_{ii}(\xi_k)$ some qualitative information can be deduced in reference to the behaviour of Taylor's microscale. In general values of λ_{11}/M appear to decrease through the interaction while values of λ_{12}/M decrease only in strong interactions with coarse grids and increase in strong interactions with fine grids or in weak interactions with any grid.

DNS results indicate a decrease in all lateral scales through a wide range of M_s. In that respect the disagreement between the experimental data and DNS remains an issue although it may be attributed to the difference in Re_λ. The Re_λ of the DNS are between 12 and 22, which is considerably lower than the values between 150 and 1300 achieved in the experiments and may be the cause of this disagreement between experiments and DNS.

The difference between experiments and DNS is also noticeable if the Reynolds number $Re_T = \overline{(\rho u_i u_i)}^2/\mu\varepsilon$ is considered, where ε the dissipation rate. Re_T in the experiments is of the order of 4×10^3 while in DNS is only 750. As a result the time scale of turbulence $T_t = q^2/\varepsilon$ and its ratio to the time scale imposed by the shock $T_{sw} = 1/S_{11}$, $R_t = T_t/T_{sw}$, are quite different between DNS and experiments.

The present results clearly show most of the changes: either attenuation or amplification of quantities involved occur for large x/M distances where the length scales of the incoming flows are large and turbulence intensities low. Thus eddies large in size with low velocity fluctuations are affected the most by the interaction with the shock.

12. Turbulence amplification through the interaction

Amplification of turbulence is one of the major features of shock–turbulence interactions. Linear analysis predicts amplification of turbulence as long as fluctuations of pressure, velocity and temperature upstream of the shock are sufficiently small that shock front distortion is considered negligible, and the Rankine–Hugoniot conditions can be linearized. DNS data for interactions with weak shocks (Lee *et al.* 1993; Hannappel & Friedrich 1995) and Euler simulations (Rotman 1991) also predict amplification of turbulence. Almost all experiments confirm qualitatively this analytical and computational result. The experiments of Jacquin *et al.* (1993) report no significant enhancement of turbulent kinetic energy. In this case, however, the deceleration in the flow upstream of the interaction because of the existence of Mach waves may have contributed to overestimating the level of turbulence upstream of the interaction. In the experimental work of Zwart, Budwig & Tavoularis (1997), a clear increase in turbulent intensities is reported, which, however, was attributed to shock wave unsteadiness.

Typically the amplification of turbulent fluctuations depends on the shock wave strength, the state of turbulence of the incoming flow before the interaction, and its level of compressibility.

Figure 19(*a*) shows the amplification ratio of the velocity vector fluctuations defined as the ratio of the standard deviation of the fluctuations downstream of the interaction σ_d to that upstream of the interaction σ_u, i.e. $G = \sigma_d/\sigma_u$. Data available for three velocity components of various experiments are plotted against the corresponding shock strength. The general trend of amplification can be depicted with the help of a polynomial best-fit line through the data. Amplification of longitudinal velocity fluctuations has been observed in all experiments. It appears that the amplification increases in interactions with higher shock strength. The data for fluctuations in the

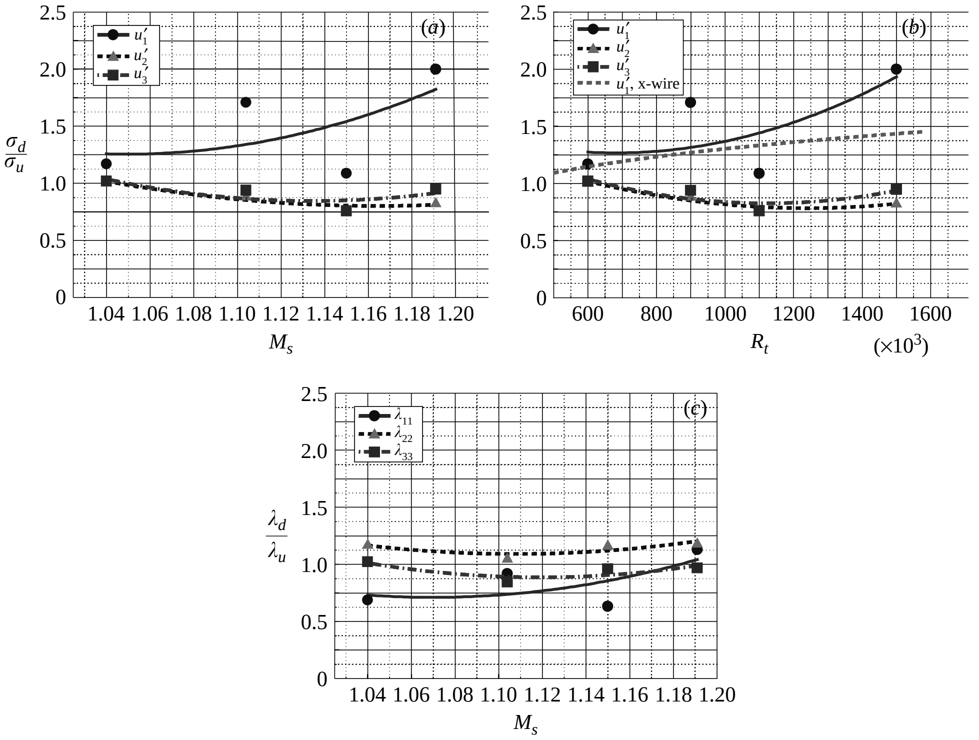

FIGURE 19. (*a*) Amplification of the velocity vector fluctuations for various interactions. (*b*) Amplification of the velocity vector fluctuations for various interactions with different time scale ratios. (*c*) Amplification of Taylor's microscales for various interactions.

lateral directions show no change or some minor attenuation through the interaction. In an axisymmetric flow, like the present one downstream of the interaction, the data in the two lateral directions should be identical. The data for the u_2 and u_3 fluctuations shown in this figure appear to be in reasonably good agreement with each other. Any difference between them can be attributed to the inherent lower degree of isotropy in the flow region downstream of the interaction, which in fact deteriorates with increasing M_s, and to the uncertainties involved in the experimental data.

A more meaningful way to present the amplification data is to plot them against the time-scale ratio $R_t = T_t/T_{sw}$, which was introduced in § 6, instead of M_s. The reason is that R_t contains information regarding the incoming isotropic flow and the interacting shock wave as opposed to M_s which is a characteristic representative of the shock wave only. Specifically, it better describes the turbulence of the incoming flow, particularly the variation of its characteristics with downstream distance. The data replotted are shown in figure 19(*b*). The general trend of the data remains the same as that of figure 19(*a*). The fluctuations of u_1 measured with a x-wire, which are shown in figure 19(*b*), agree well with the corresponding data obtained with the vorticity probe. They also indicate that amplification of longitudinal velocity fluctuations increases with increasing R_t.

Of interest is the behaviour of the fluctuations of the velocity gradient tensor $A_{ij} = \partial U_i/\partial x_j$. Since two measurements of velocity U_i at close locations x_j, $x_j + \Delta x_j$ have been attempted the velocity gradient tensor can be estimated by $\Delta U_i/\Delta x_j$ where $\Delta U_i = U_i(x_j + \Delta x_j) - U_i(x_j)$. According to the work of Honkan & Andreopoulos

(1997) on the physics of the structure function, it appears that

$$\left[\overline{\left(\frac{\Delta U_i}{\Delta x_j}\right)^2}\right]^{1/2} = \frac{\left[\overline{U_i^2(x_j)}\right]^{1/2}}{\Delta x_j}[(1-r_u)^2 + 2r_u(1-r_{ii})]^{1/2} \tag{12.1}$$

where

$$r_u = \left[\frac{\overline{U_i^2(x_j+\Delta x_j)}}{\overline{U_i^2(x_j)}}\right]^{1/2}$$

and r_{ii} is the cross-correlation function

$$r = r_{ii}(\Delta x_j) = \overline{U_i(x_j)U_i(x_j+\Delta x_j)}\big/\big(\overline{U_i^2(x_j)}\big)^{1/2}\big(\overline{U_i^2(x_j+\Delta x_j)}\big)^{1/2}.$$

The above relation (12.1) indicates that the r.m.s. value of the quantity $\Delta U_i/\Delta x_j$ depends among other quantities on $(1-r_u)$ and $(1-r_{ii})$. The first quantity is a measure of the inhomogeneity of the r.m.s. while the second one indicates the uncorrelated part between the two velocity fluctuations at x_j and $x_j+\Delta x_j$. It can be argued that for small separations Δx_j, r_u does not vary significantly. In the lateral directions of the present flow it remains 1 and in the longitudinal direction it changes slowly. For instance, by considering equation (6.1) it appears that

$$r_u^2 = \left[1 + \frac{\Delta x_j}{x_j - x_0}\right]^{-n}.$$

For $\Delta x_j = 1$ mm and $x_j - x_0 = 100$ mm then r_u obtains values close to 0.998. Therefore it is very reasonable to assume that the term $(1-r_u)^2$ reaches very small values and it can be ignored. This yields the following relation:

$$\left[\overline{\left(\frac{\Delta U_i}{\Delta x_j}\right)^2}\right]^{1/2} = \frac{\left[\overline{U_i^2(x_j)}\right]^{1/2}}{\Delta x_j}[2r_u(1-r_{ii})]^{1/2} \tag{12.2}$$

which indicates that most contributions to $\Delta U_i/\Delta x_j$ come from the uncorrelated part of the two velocity signals. It is known that the existence of small scales in the flow decrease r_{ii}. On the other hand two sinusoidal signals with a phase shift will also result in correlation coefficient r_{ii} lower than 1. Thus contributions to $\Delta U_i/\Delta x_j$ may come from the high-wavenumber part of the spectrum or out-of-phase large eddies in the low-wavenumber part.

The limit of equation (12.1) when Δx_j approaches zero is also of interest in the present considerations because it represents the case with ideal spatial resolution in the measurements of velocity gradient tensor. This limit should be compared to equation (12.1) itself since it represents the actual practice in these measurements. As Δx_j approaches zero, both r_u and r_{ii} approach 1 and thus the limit appears to become indefinite. After applying L' Hospital's rule, the following relation can be obtained:

$$\overline{\left(\frac{\Delta U_i}{\Delta x_j}\right)^2_{\Delta x_j \to 0}} = \frac{\left[\overline{U_i^2(x_j)}\right]}{\lambda_{ij}^2}\left[1 + \lambda_{ij}^2\left(\frac{\partial r_u}{\partial \Delta x_j}\right)^2\right] \tag{12.3}$$

where λ_{ij} is Taylor's microscale.

Thus this limit determines the highest attainable value under an ideal probe resolution. The second term in the square bracket of this equation can attain values that depend on the location x_j and direction Δx_j. In general this ratio is smaller than 1 and in most cases it can be neglected. For instance in the lateral direction of the

σ_d/σ_u	$M_s = 1.04$	$M_s = 1.10$	$M_s = 1.15$	$M_s = 1.19$
$(\mathrm{d}u_1/\mathrm{d}x_1)'$	1.7	1.86	1.5	1.93
$(\mathrm{d}u_2/\mathrm{d}x_1)'$	1.5	1.32	1.14	1.28
$(\mathrm{d}u_3/\mathrm{d}x_1)'$	1.61	1.54	1.35	1.6
$(\mathrm{d}u_1/\mathrm{d}x_2)'$	0.85	1.06	0.84	0.96
$(\mathrm{d}u_2/\mathrm{d}x_2)'$	0.74	0.84	0.65	0.7
$(\mathrm{d}u_3/\mathrm{d}x_2)'$	0.98	0.91	0.82	0.78
ω_1'	0.88	0.95	0.8	0.78
ω_2'	1.26	1.40	1.10	1.38
ω_3'	1.24	1.17	1.12	1.10
$\omega_k\omega_k'$	1.10	1.29	0.93	1.02
$s_{kk}s_{kk}'$	1.37	1.41	1.60	1.29
s_{kk}'	1.51	1.12	1.18	1.02
$s_{11}\omega_1'$	1.26	1.14	1.06	1.61
$s_{12}\omega_2'$	1.79	1.29	1.10	1.75
$s_{13}\omega_3'$	1.80	1.48	1.34	1.77
$s_{21}\omega_1'$	1.32	1.48	1.12	1.22
$s_{22}\omega_2'$	0.86	0.74	0.73	1.02
$s_{23}\omega_3'$	1.05	0.95	0.73	1.05
$s_{1k}\omega_k'$	1.30	1.19	1.15	1.64
$s_{2k}\omega_k'$	1.02	0.88	0.88	1.06
$s_{3k}\omega_k'$	1.07	1.14	0.9	1.24
$s_{kk}\omega_1'$	1.25	1.01	0.92	1.06
$s_{kk}\omega_2'$	1.73	1.60	1.18	1.79
$s_{kk}\omega_3'$	1.73	1.36	1.28	1.59

TABLE 5. Data of amplification of r.m.s. of fluctuations of various turbulent quantities.

present flow it is zero while in the longitudinal direction it is of the order of 10^{-2} to 10^{-3}.

In cases where this term can be omitted then (12.3) becomes

$$\overline{\left(\frac{\Delta U_i}{\Delta x_j}\right)^2_{\Delta x_j \to 0}} = \frac{\left[\overline{U_i^2(x_j)}\right]}{\lambda_{ij}^2} \tag{12.4}$$

If U_i is replaced by its fluctuating part u_i then this relation is the same as what is considered as an order of magnitude value for vorticity fluctuations by Tennekes & Lumley (1972).

Typical data for the amplification ratio of six individual terms of the velocity gradient tensor $A_{ij} = \partial U_i/\partial x_j = \partial u_i/\partial x_j$ are shown in table 5. Data for velocity gradients in the lateral direction x_3 are not shown since they exhibit the same behaviour as those in the x_2-direction, because of the axisymmetry of the interaction.

The data in table 5 suggest that the fluctuations of all velocity gradients in the longitudinal direction, i.e. $(\mathrm{d}u_i/\mathrm{d}x_1)$, are amplified downstream of the interaction by an average amount of about 50%. The data of $(\mathrm{d}u_1/\mathrm{d}x_1)$ also indicate a weak increase with increasing shock strength M_s or time ratio R_t. The data of $(\mathrm{d}u_2/\mathrm{d}x_1)$ and $(\mathrm{d}u_3/\mathrm{d}x_1)$ show no strong dependence on M_s or R_t. Due to the axisymmetric character of the interaction, these data should be identical. There is a 15% difference between them that can be attributed to the uncertainties involved in the measurements of these quantities and to the deterioration of isotropy downstream of the shock interaction with increasing M_s or R_t.

Fluctuations of the velocity gradients in the lateral directions show no change or a minor reduction through the interaction. Fluctuations of the off-diagonal terms $(\mathrm{d}u_1/\mathrm{d}x_2)$ and $(\mathrm{d}u_3/\mathrm{d}x_2)$ show no substantial change while fluctuations of the diagonal term $(\mathrm{d}u_2/\mathrm{d}x_2)$ are reduced by about 25%. Thus $(\mathrm{d}u_2/\mathrm{d}x_2)'$ and $(\mathrm{d}u_3/\mathrm{d}x_3)'$ decrease after the shock interaction while $(\mathrm{d}u_1/\mathrm{d}x_1)'$ increases substantially and dilatation s'_{kk} increases modestly.

These characteristics of the fluctuating components of the velocity gradient tensor through the interaction affect the behaviour of Taylor's microscale through the interaction. As shown in figure 19(*c*), where data for λ_{11}, λ_{22} and λ_{33} are plotted, Taylor's microscale in the longitudinal direction λ_{11} is reduced substantially after the interaction while λ_{22} and λ_{33} show no significant change. All microscales indicate no meaningful variation with M_s or R_t. In that respect, the behaviour of Taylor's microscales during sudden compression appear to be similar to that of the integral length scales: they are reduced in the longitudinal directions while their extent in the lateral directions more or less remains the same.

The data on amplification of fluctuations of the vorticity vector are also tabulated in table 5. Root mean square values of the lateral vorticity components ω'_2 and ω'_3 indicate a 25% amplification on average, which appears to be very weakly dependent on M_s or R_t. The transmission of the longitudinal velocity fluctuations ω_1 through the shock appears to be less affected by the interaction than the fluctuations of the lateral components ω_2 and ω_3. The data show a minor reduction in ω'_1 that is compatible with the minor reductions observed in the fluctuations of the lateral velocity gradients $(\mathrm{d}u_3/\mathrm{d}x_2)$ and $(\mathrm{d}u_2/\mathrm{d}x_3)$.

The effects of the shock interaction on the fluctuations of enstrophy, $\omega_k\omega_k$, dilatation, s_{kk}, and dilatational dissipation rate, $s_{kk}s_{kk}$, are also shown in table 5. A minor increase in $\omega_k\omega'_k$ has been estimated from the present data. Dilatational fluctuations of s_{kk} and $s_{kk}\,s_{kk}$ appear to be amplified through the interaction more than $\omega_k\omega_k$ fluctuations.

Amplification of fluctuations of each of the terms of the longitudinal component of the stretching and tilting vector $s_{1k}\omega_k$ are also evident from the data shown in table 5. It appears that all terms are amplified through the interaction by various amounts. The stretching/compressing term $s_{11}\omega_1$ exhibits the least amplification while the other two terms $s_{12}\omega_2$ and $s_{13}\omega_3$ experience the most. The situation, however, is different in the lateral direction, where the data of table 5 show that $s_{21}\omega'_1$ is amplified by about 25%, $s_{22}\omega'_2$ is reduced by about 20% and $\mathrm{s}_{23}\omega'_3$ is very little affected by the interaction. Amplification data of fluctuations of the resultant components $s_{1k}\omega_k$, $s_{2k}\omega_k$ and $s_{3k}\omega_k$ are also shown in table 5. The r.m.s. values of the longitudinal component $s_{1k}\omega'_k$ are amplified by about 25%, while the r.m.s. values of stretching and tilting in the lateral directions $s_{2k}\omega'_k$ and $s_{3k}\omega'_k$ show only small changes from their upstream values.

Amplification data of fluctuations of the dilatational source term $s_{kk}\omega_i$ are shown in table 5. The results indicate significant amplification of lateral vorticity components generated by dilatation, $s_{kk}\omega_2$, $s_{kk}\omega_3$, while no change can be discerned in the r.m.s. values of $s_{kk}\omega'_1$.

The present experimental data on amplification of velocity and vorticity fluctuations through the shock wave interaction have been compared with theoretical data derived from LIA and RDT as well as with results from DNS. The results of this comparison are shown in figures 20(*a*) and 20(*b*), where the amplification ratio of the variance of velocity and vorticity fluctuations is plotted respectively for various values of shock wave strength, M_s. LIA and DNS data shown in these figures are the results obtained by Lee *et al.* (1993).

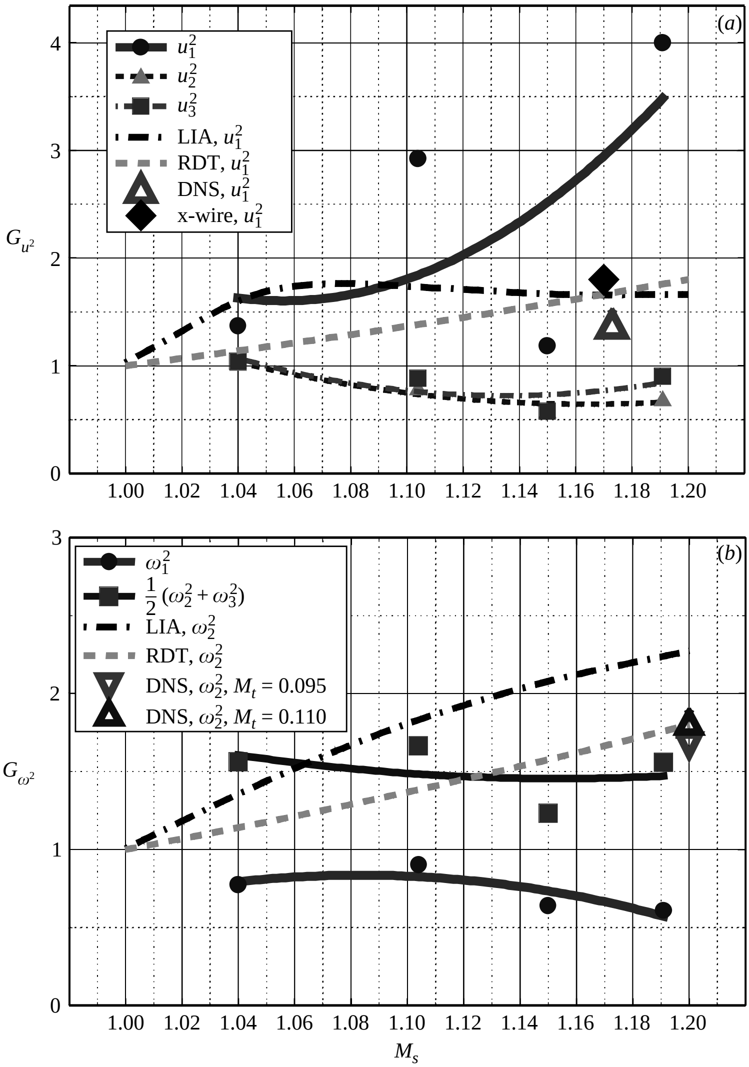

FIGURE 20. Amplification of (*a*) velocity and (*b*) vorticity fluctuations. LIA of Lee *et al.* (1993); RDT of Jacquin *et al.* (1993); DNS of Lee *et al.* (1993).

The RDT of Jacquin *et al.* (1993) indicates that the crucial parameter which describes turbulence subjected to rapid compression is the ratio of the upstream acoustic time scale $(\alpha_u k_u)^{-1}$ to the time scale of the deformation rate S_{11}^{-1} where α_u is the speed of sound and k_u is the wavenumber corresponding to a characteristic length scale L_u of the upstream turbulence, $L_u = k_u^{-1}$. According to Durbin & Zeman (1992) this ratio $\Delta m = S_{11} L_u / \alpha_u$ can be interpreted as a change in a characteristic Mach number due to the applied distortion across an eddy of size L_u. If L_u is chosen to be the dissipation length scale L_ε then $\Delta m = M_t R_t$. Values of R_t in the present work are of order 10^6 while values of M_t are of order 10^{-2}. Thus Δm reaches values of order 10^4. If the integral length scale of the incoming turbulence L_{11} is used instead of L_ε then Δm is of order 10^2. In either case, it appears that $\Delta m \gg 1$ in all experiments and therefore a dilatational regime holds where longitudinal velocity fluctuations are directly fed by the compression without the damping effects by the pressure term. Thus, according to Jacquin *et al.* (1993) for $\Delta m^2 \gg 1$ the rapidity of the distortion does not allow any correlation between pressure and velocity fluctuations, a situation which precludes the damping effects of pressure and therefore maximum amplification takes place. This leads to the following simple relations for the amplifications of longitudinal velocity and lateral vorticity fluctuations: $G_{u_1^2} = C^2$ and $G_{\omega_2^2} = C^2$, where C is the density ratio $C = \rho_d/\rho_u$. Then $G_{q^2} = \frac{1}{3}[2 + C^2]$ and $G_{\omega^2} = \frac{1}{3}[1 + 2C^2]$ are the amplification ratios for the turbulent kinetic energy and enstrophy respectively. It should be noted that these expressions are valid for solenoidal and non-solenoidal initial conditions. The results of the RDT are also plotted in figures 20(*a*) and 20(*b*). The density ratio in the present experiments, where the vorticity measurements were carried out, had values in the range of 1.12 to 1.37. Density ratios up to 1.7 were also measured in other experiments where conventional hot-wire probes were used.

LIA predicts higher amplification of velocity and vorticity fluctuations than RDT at low M_s and assumes no changes in the velocity components parallel to the shock front, u_2 and u_3. LIA results seem to level off for $M_s > 1.06$, while RTD predicts continuous increase.

The present data on amplification of velocity fluctuations agree with the predictions of LIA and RDT in the range of low M_s. At higher M_s, the data obtained with the vorticity probe show values of $G_{u_1^2}$ that are considerably higher than those predicted. The data amplification of vorticity fluctuations, however, agree well with the theoretical results in the range of the measured values of M_s.

Both LIA and RDT predict that lateral vorticity fluctuations increase with the shock strength after the interaction with the shock wave while the experimental data shown in figure 20(*b*) indicate no clear trend confirming this.

LIA is based on the Rankine–Hugoniot jump relations and therefore it has the potential to capture the physics of the interaction better than RDT, which ignores the basic interaction between the flow and the shock.

The DNS data of Hannappel & Friedrich (1995) show that the amplification of vorticity fluctuations in the lateral direction increases with compressibility in the upstream flow while the amplification of longitudinal velocity fluctuations is reduced by the same effect. These authors also found that longitudinal vorticity fluctuations are slightly reduced through the shock, as has been found in the present experiments.

The early work of Honkan & Andreopoulos (1992) showed that amplification of u_{rms}, G_u, also depends on the turbulence intensity and length scale of the incoming isotropic turbulence. The present work as well the work of Briassulis & Andreopoulos (1996) confirm this finding. The amplification of turbulent kinetic energy across shocks seems to decrease with increasing M_t. Both experimental data from the abovementioned studies and the DNS data of Lee *et al.* (1993) and Hannappel & Friedrich (1995) agree with this finding. Thus the outcome of the shock–turbulence interaction depends also on the compressibility level of the incoming flow.

The effect of the shock strength on the velocity fluctuations is shown in figure 21(*a*). For the 1 × 1 grid, it appears that the amplification of the standard deviation of turbulence fluctuations increases with downstream distance for a given flow case and interaction. Thus, turbulence amplification depends on the evolution of the flow upstream. As M_u increases, G_u also increases. For finer grids the effects of shock interaction are felt differently. For the 2 × 2 grid for instance, the data show that in the first case of a practically incompressible upstream flow interacting with a rather weak shock, amplification of turbulence occurs at $x/M > 35$. The amplification is greater when M_u increases to 0.436. However, when compressibility effects in the upstream flow start to become important no amplification takes place (G_u is about 1).

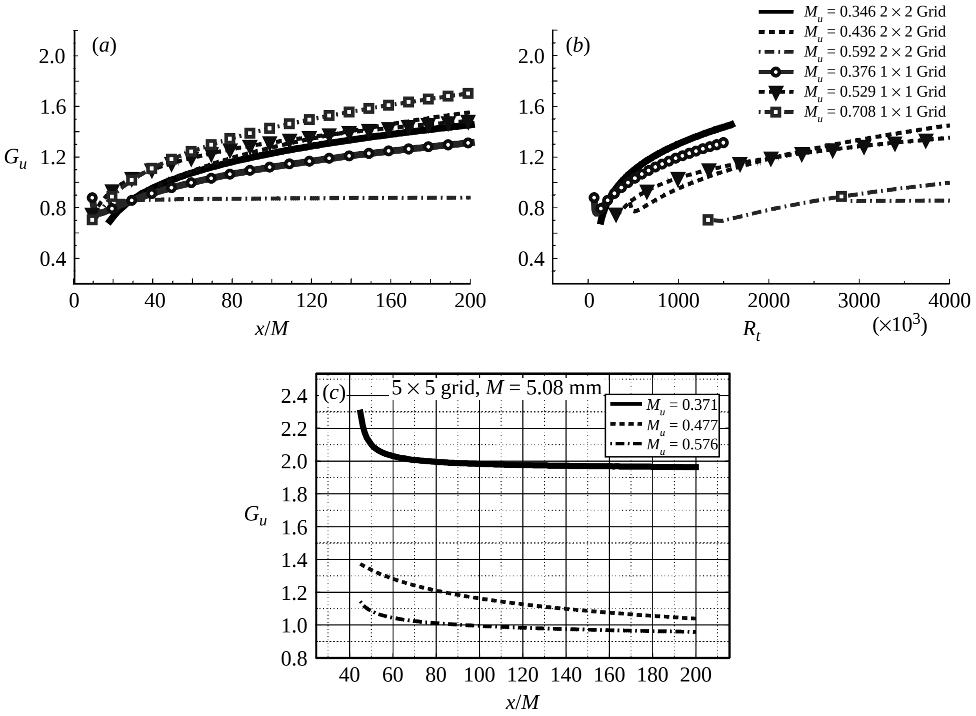

FIGURE 21. (*a*) Effects of upstream flow compressibility and shock strength on amplification of velocity fluctuations along the flow field in various interactions. (*b*) Amplification of velocity flucuations along the flow field in various interactions with different time scale ratio R_t. (*c*) Amplification of velocity fluctuations along the flow field in various interactions with different Mach numbers.

The data shown in figure 21(*a*) indicate that G_u is not constant along the flow field for a given shock wave strength, M_s. In an effort to better collapse the data shown in figure 21(*a*) a different scaling has been attempted, namely the time ratio R_t has been used instead of x/M. The results are shown in figure 21(*b*). There is some evidence indicating that the data of G_u for different grids and at roughly the same M_u collapse more closely with each other with this scaling than before. However, this scaling is inadequate in bringing closer the data of G_u obtained at different M_u.

Some more dramatic effects of compressibility are illustrated in figure 21(*c*), where the amplification G_u is plotted for the case of a finer grid with mesh size 5 × 5. The interaction of a weak shock with a practically incompressible turbulent flow produces the highest amplification of velocity fluctuations with G_u reaching a value close to 2. As M_u increases, G_u decreases and at $M_u = 0.576$ a slight attenuation occurs at downstream distances. It is therefore plausible to conclude that for high shock strengths compressibility effects control the velocity fluctuations, which are generated by fine grids, and no amplification of turbulent kinetic energy is observed.

Hannappel & Friedrich (1995) have also shown in their DNS work that compressibility effects upstream reduce turbulence amplification significantly. The LIA of Ribner, which was initially developed for an incompressible isotropic turbulent field, predicts amplification of turbulence fluctuations. Mahesh *et al.* (1997) have shown recently that LIA as well as DNS may show a complete suppression of amplification of kinetic energy if the upstream correlation between velocity and temperature

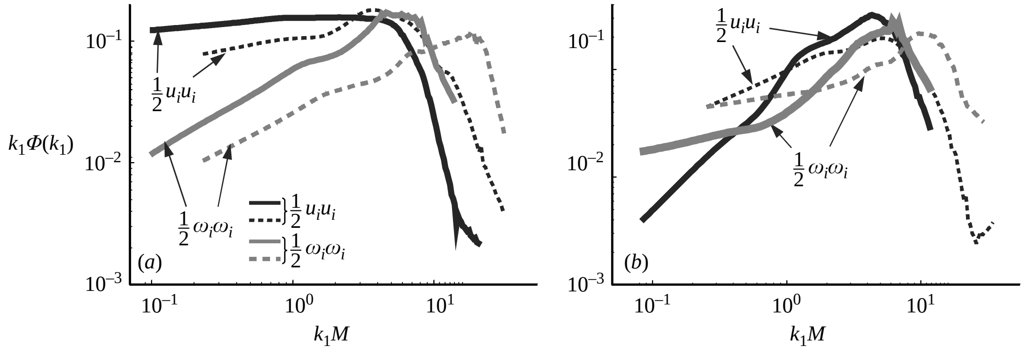

FIGURE 22. Wavenumber-weighted power spectral densities of turbulent kinetic energy, $1/2u_iu_i$ and enstrophy, $1/2\omega_i\omega_i$ upstream and downstream of the interaction in the case of (*a*) $M_s = 1.04$ and $M = 12.7$ mm, (*b*) $M_s = 1.115$ and $M = 12.7$ mm. Solid lines, upstream values; dotted lines, downstream values.

fluctuations is positive. It is therefore possible that in the case of very fine grids and high-Mach-number flows, where the dissipation rate of turbulent kinetic energy is so high, entropy or pressure fluctuations may be responsible for completely suppressing turbulence amplification.

In the work of Briassulis (1996) amplification of velocity fluctuations after the interaction was found in all cases involving turbulence produced by coarse grids. This amplification increases with shock strength and flow Mach number. In the case of fine grids, amplification was found in all interactions with low M_u, while at higher M_u it was reduced or no amplification of turbulence was evident. These results indicate that the outcome of the interaction depends strongly on the upstream turbulence of the flow.

13. Spectral densities

Some further insight into the evolution of turbulence through the rapid compression by a shock wave can be obtained by examining the one-dimensional wavenumber spectra (power spectral densities) of turbulent kinetic energy and of enstrophy, which describe the translational kinetic energy relative to the mean and the rotational kinetic energy respectively. Figures 22(*a*) and 22(*b*) show spectra of $1/2u_iu_i$ and $1/2\omega_i\omega_i$ upstream and downstream of the interaction obtained for two different interactions with $M_s = 1.04$ and 1.115 respectively. These spectra have been computed from frequency spectra after invoking Taylor's hypothesis with convection velocities being the mean velocities U_u and U_d upstream and downstream of the shock wave regions. This is based on the assumption that the frequency of the waves, ω, remains unchanged by the interaction and that the associated wavenumber, k_1, changes to satisfy the dispersion relation $\omega - k_1U_c = 0$ where U_c is the convection velocity. Because of the difference in U_c the upstream and downstream wavenumber range will be different. The present choice of convection velocities refers to the laboratory system of reference as opposed to the alternative one moving with the shock, which requires different convection velocities. Values of the streamwise wavenumber k_1 have been non-dimensionalized by the mesh size M.

The upper limit in the wavenumber scales is defined by the resolution of the instrumentation and the lower limit, i.e. the larger eddies are defined by the shock tube diameter D. Thus the ratio of the largest to smallest resolvable scales is about 300:1.

In the case of $M_u = 0.308$ which is shown in figure 22(*a*), the maximum value of the spectral density of turbulent kinetic energy occurs at approximately $k_1 M = 4.5$ while the maximum value of the spectral density of enstrophy occurs at about $k_1 M = 7$. This difference in the maxima of spectral energies indicates a shift towards higher wavenumbers of enstrophy fluctuations, which suggests that they are mainly a result of a greater proportion of contributions by the smaller scales whereas the kinetic energy contains contributions from relatively larger eddies.

Through the interaction the spectral content of both turbulent kinetic energy and enstrophy changes significantly. The most revealing pattern is that, after the interaction, the part of the spectrum with most of the spectral energy moves to higher wavenumbers. This clearly indicates an amplification of turbulent kinetic energy. The spectra of enstrophy also show a similar shift of energy towards higher wavenumbers. The maximum value of p.s.d. occurs at $k_1 M = 20$ an almost threefold shift from the upstream value of 7. It is also interesting to observe that the larger turbulent intensities with the larger turbulent scale, i.e. small k_1, are suppressed by the interaction.

In the case of $M_u = 0.388$, shown in figure 22(*b*), the maximum of turbulent kinetic energy is found to occur at about the same wavenumber as in the case of $M_u = 0.308$, i.e. at $k_1 M = 4.5$, while the maximum energy of enstrophy occurs at a lower wavenumber $k_1 M = 5.8$. Once more, the data show that there is a shift towards higher wavenumbers in the case of enstrophy maxima. However, it appears that increasing M_u reduces the difference between the wavenumbers where the maxima of kinetic energy and enstrophy occur. If one considers that the peak in turbulent kinetic energy represents the size of large energy-containing eddies and that the peak in enstrophy represents mostly small energy-dissipating eddies then it would be expected that this difference or shift increases with increasing Reynolds number. The fact that this shift decreases with Mach number in the present case indicates that the effect of M_u in reducing this difference becomes stronger than the effect of Reynolds in increasing it. There is also a smaller shift in wavenumber of the maximum values after the interaction. In the case of enstrophy the maximum occurs at $k_1 M = 12$ which represents a twofold increase of the upstream wavenumber of 5.7.

Of interest is the wavenumber k_c where the two p.s.d. curves before and after the interaction cross each other. Waves with $k_1 > k_c$ will be amplified through the interaction and waves with $k_1 < k_c$ will be suppressed. In general these two curves may intersect at two, one or zero points. Intersections in the low-wavenumber region are of limited use because they are influenced by the size of the experimental facility, in the present case the shock tube diameter D. Intersections in the high-wavenumber regions are of more value. In the present case, it appears that a rough estimate for both data sets is $k_c M \approx 10$. This value implies that for the corresponding wavelength λ_c, $M/\lambda_c = k_c M/2\pi \approx 1.6$ and that $D/\lambda_c = k_c D/2\pi \approx 38$. Thus the cross-over wavelength λ_c is very closely related to the mesh size M. For waves with wavelength $\lambda < \lambda_c$ amplification will take place and all waves with $\lambda > \lambda_c$ will be suppressed. In addition this information indicates that 38 wavelengths fit in the shock tube diameter, a condition necessary for the use of the infinite-shock-wave assumption present in LIA.

14. Shock wave modifications and the mutual interaction

One key point in the interpretation of the present results may be the possible deformation of the shock front due to the incoming turbulence. DNS and LIA can account for such perturbations while RDT is unable to do so. Some evidence possibly

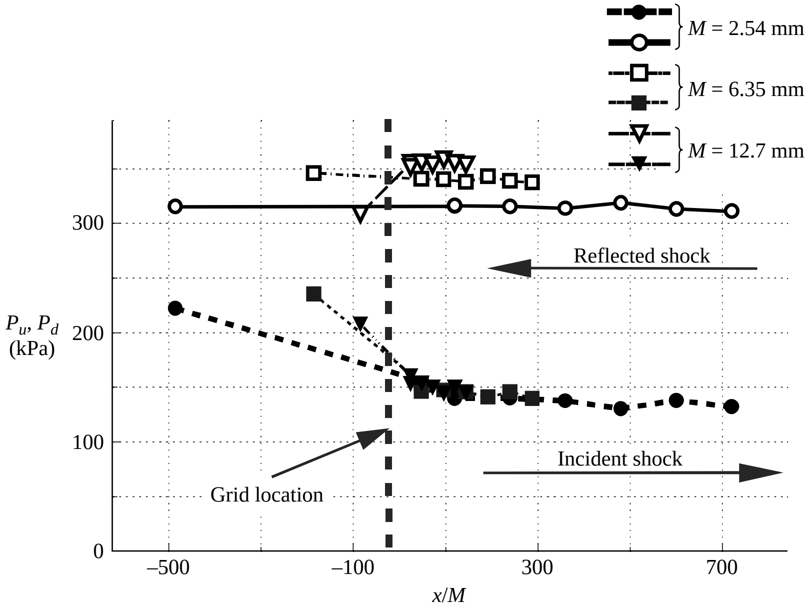

FIGURE 23. Mean pressure distribution along the working section for various flows with different grids. Filled and open symbols correspond to flows upstream and downstream of the shock wave, P_u and P_d, respectively.

showing the effects of turbulence on the shock wave can be found in the work of Xanthos *et al.* (2002) where the influence of grid solidity and mesh size on the transmitted shock wave has been investigated. Their mean pressure data along the working section are plotted against their normalized distance from the grid location in figure 23. In all experiments with various grid sizes, the transmitted shock through the grid had the same strength. This was achieved by slightly readjusting the incident shock strength to account for the difference in pressure drops across the various grids so that the pressure behind the transmitted shock was practically the same. In this way the shock strength before the reflection off the endwall and the subsequent interaction with the incoming turbulence was the same in most of these experiments. The data in figure 23 show that the pressure downstream of the grid and after the passage of the transmitted shock remains the same in all experiments with the three different grid sizes. The present data also show that the pressure behind the shock does not exhibit any gradient along the working section after the passage of the incident or the reflected shock wave.

It is very interesting to observe, in figure 23, that the mean pressure behind the reflected shock is not the same in all experiments with the same incident shock strength (P_2/P_1). It appears that the reflected shock strength, P_5/P_1, attenuates more in the case of fine grids. Thus, the pressure jump due to further compression by the reflected shock is less than the value predicted by the inviscid theory. It is obvious that there exists a substantial grid dependence of pressure losses, the cause of which has to be further explored.

Three possible explanations have been considered for this behaviour. The first one is based on a possibly long-lasting distortion of the shock front, which occurred during its passage through the grid. Numerical simulations have shown that the shock wave is considerably distorted when it is transmitted through the grid. Its front distortion scales with the mesh size M. It is possible that this distortion does not decay quickly and that it has a long-lasting memory. However, our experience with shock distortions, based on experimental and computational results, indicates that the shock wave becomes planar within two to three shock-tube diameters even after strong reflections over three-dimensional surfaces. In addition, it is rather unlikely that the distorted shock wave retains the grid signature after its reflection off the endwall of the shock tube.

As a second explanation, the behaviour of the present data may be attributed to the different viscous losses, occurring during the reflection of the shock in the presence of free-stream turbulence. However, decaying turbulence generated by the grids is not present during the reflection at the endwall because it travels with the flow speed, which is considerably lower than the speed of the shock wave. Thus, the shock wave and the front of the decaying turbulence cannot be at the endwall location at the same time. The turbulence, which is generated inside the unsteady boundary layers developing over the shock tube wall behind the travelling shock and which is present during the reflection, has not passed through the grid and therefore does not carry any grid signature.

The most plausible interpretation of this behaviour is the strong interaction of the reflected shock wave with the grid-generated turbulent field, which takes place away from the endwall. The first encounter of the reflected shock with the decaying turbulence occurs away from the grid where the length scales of turbulence are large and the velocity fluctuations are small. As a result of this interaction the shock wave is distorted considerably by the large eddies of the flow and velocity fluctuations increase as a direct consequence of the Rankine–Hugoniot conditions. Thus the interaction between the shock wave and the turbulence field appears to be mutual. The shock wave retains its strength as it travels through the turbulent flow field, as is evident from the data for mean pressure behind the reflected shock, which show no substantial pressure gradient (see figure 23). It is believed, however, that the majority of the loss of its strength occurs in the early stages of the interaction where the shock front first meets the front of the decaying turbulence at a location far from the grid, where length scales are large and intensities are low and where most of the viscous effects are present. Apparently these viscous effects are stronger in the case of finer than coarse grids.

At this moment it is not clear how a perturbed shock front will affect the interaction. It is expected that any shock front corrugations will scale with the local velocity and length scales of the most energetic eddies. The work of Lee *et al.* (1992) has indicated that the r.m.s. of the local amplitude of the shock front displacement, ξ_{rms}, the r.m.s. of its local inclination σ_{rms} and the r.m.s. of the local curvature $\kappa_{2,rms}$ are reduced fast with increased shock strength M_s. This work has indicated that ξ_{rms} scales with $u'_1/U_u k_u^{-1}$, σ_{rms} scales with u'_1/U_u and $\kappa_{2,rms}$ scales with $u'_1/U_u k_u$ where u'_1/U_u is the local turbulence intensity and k_u is the wavenumber of the most energetic eddies in the local upstream flow. Since u'_1/U_u is proportional to M_t/M_u, it appears that the three characteristic parameters of the shock front distortion are reduced with increased M_u and increase with higher M_t. If we assume that $k_u^{-1} = L_u$ and $L_u \propto L_\varepsilon \propto [x - x_0]^{1-n/2}$ then $\xi_{rms} \propto [x - x_0]^{1-n}$, $\sigma_{rms} \propto [x - x_0]^{-n/2}$ and $\kappa_{2,rms} \propto [x - x_0]^{-1}$. Thus the inclination and curvature of the shock distortions are reduced downstream of the grid, therefore baroclinic effects which could be generated at the shock front are not expected to be important. This argumentation leads to the conclusion that the most plausible explanation for the pressure losses shown in figure 23 is viscous effects and not distortions of the shock front by the incoming turbulence.

15. Concluding remarks

An attempt has been made to investigate experimentally the effects of rapid compression caused by a moving shock wave on isotropic turbulence in a large-scale shock tube facility by employing multiple hot-wire probes of various types and related instrumentation with high spatial and temporal resolution. The flow field was generated by using a variety of grids of rectangular pattern of different mesh size. The Reynolds number of the flow based on the mesh size, Re_M, ranged from 50 000 to 400 000 while the turbulent Reynolds number Re_λ based on Taylor's microscale was between 200 and 1300, which constitutes one of the highest scales ever achieved in a laboratory flow. The range of Mach number of the flows investigated was between 0.3 and 0.6. In that respect some of the interactions with incoming flows at $M_u = 0.3$ are considered as interactions with an almost incompressible flow. Interactions with shock wave Mach numbers M_s ranging from 1.04 to 1.392 were achieved in the present investigations. The ratio of the eddy turnover time to that of the strain rate of the interaction reached values in the range of 0.5×10^6 to 5×10^6.

A custom-designed vorticity probe was used to measure for the first time the rate-of-strain, the rate-of-rotation and the velocity-gradient tensors in several of the present flows. Testing and validation of the probe and its eventual use in the shock tube flow field were formidable tasks. The difficulties associated with the measurements of velocity gradients in non-isothermal flows are discussed in BAA. Issues related to calibration, data analysis and spatial and temporal resolutions appeared to be the most challenging.

A custom-made rake of hot-wire probes was also used to measure spatial correlations inside the flow fields, which provided estimates of the integral length scales in the lateral and longitudinal directions.

Integral length scales were reduced after the interaction with the shock in all investigated flow cases. Taylor's microscales were also reduced downstream of the interaction. The integral length scales in the lateral direction increased at low Mach numbers and decrease during strong interactions. It appears that at the weakest of the present interactions, turbulent eddies are drastically compressed in the longitudinal direction while their extent in the normal direction remains relatively the same. As the shock strength increases the lateral integral length scale increases while the longitudinal decreases. At the strongest interaction of the present flow cases turbulent eddies are compressed in both directions. However, even at the highest Mach number the issue is more complicated since amplification of the lateral scales has been observed in flows with fine grids.

Amplification of longitudinal velocity fluctuations has been observed in all experiments. It appears that the amplification increases in interactions with higher shock strength. The data of velocity fluctuations in the lateral directions show no change or some minor attenuation through the interaction. In the case of fine grids, amplification of longitudinal velocity fluctuations was found in all interactions with low M_u, while at higher M_u they were reduced, or no amplification of turbulence was evident. These results indicate that the outcome of the interaction depends strongly on the upstream turbulence of the flow.

The present results clearly show that most of the cases, either attenuation or amplification, occur at large x/M distances where length scales of the incoming flow are high and turbulence intensities are low. Thus eddies large in size with low velocity fluctuations are affected most by the interaction with the shock.

Fluctuations of all velocity gradients in the longitudinal direction are amplified significantly downstream of the interaction. Fluctuations of the velocity gradients in the lateral directions show no change or a minor reduction through the interaction. Root mean square values of the lateral vorticity components indicate a 25% amplification on average, which appears to be very weakly dependent on the shock strength. The transmission of the longitudinal vorticity fluctuations through the shock appears to be less affected by the interaction than the fluctuations of the lateral components.

Mean helicity is zero before and after the interaction with the shock while its fluctuations are amplified. A weak preferential alignment between vorticity and velocity vectors which exists in the upstream region vanishes after the interaction. The interaction, however, does not affect the alignment between vorticity and its stretching vector which appears to have a preferred value mostly of 0° or 180°.

A spectral analysis of fluctuations of turbulent kinetic energy and enstrophy revealed that the interaction of the shock wave brought about an enhancement of fluctuations of the smaller scales. The peak spectral amplitude of this enhancement occurred at a wavelength corresponding to the scale of the grid mesh size and therefore it was also related to the initial turbulence level. The spectral changes in enstrophy after the interaction showed the clearest evidence of a shift of the rotational energy to higher wavenumbers, and therefore to smaller scales.

A study of the vorticity stretching process revealed that this process is not continuous and it displays a strong bursting character. In most cases, enhanced stretching fluctuations and bursting behaviour were found after the flow had interacted with the shock wave. This was seen most clearly when the smaller mesh size grid was used at the highest Mach number investigated. Direct measurement of the dissipation, possible only through the availability of all the instantaneous velocity gradients, showed that the dissipation increased through the interaction. This effect was felt more at the lower Mach numbers investigated.

The bursting behaviour of the vortex stretching/tilting vector was also observed in the time-dependent signals of enstrophy, dissipation rate and dilatational stretching vector, which exhibited a rather strong intermittent behaviour that is characterized by high-amplitude bursts with values up to 8 times their r.m.s. within periods of less violent and longer-lived events. Several of these bursts are evident in all the signals at the same time, suggesting the existence of a dynamical flow phenomenon as a common cause. The relation between enstrophy and dissipation rate was further explored during these dynamically significant processes. The present data show that dissipation dominates the flow motions more than enstrophy. Some weak activity of events indicative of the existence of non-dissipative vortex tubes has been observed. Substantial irrotational dissipative motions are also present. Downstream of the interaction, the ranges of enstrophy and dissipation rate increase. Events indicative of non-dissipative vortex tubes and irrotational dissipative motions are more intense in this region than upstream of the shock. There is also significant increase in the number of events with intense rotational and dissipative motions. Most of the flow motions with rotational activities are associated with small but non-negligible dilatational dissipation.

The present results strongly suggest that the events that cause the high-amplitude signals may be signatures of structures with strong vorticity and of small size, often called ‘worms’, as was found by Kerr (1985), She, Jackson & Orszag (1991), Ruetsch & Maxey (1991). These structures, depending on their orientation, in general are affected strongly by the shock interaction.

The financial support provided was by NASA Grants #NAG-1590 and NAG3-2163 monitored by Mr Dennis Bushnell and Dr David O. Davis. The authors would like to thank the referees for their comments.

REFERENCES

AGUI, J. H. 1998 Shock wave interactions with turbulence and vortices. PhD thesis, The City University of New York.

AGUI, J. H. & ANDREOPOULOS, Y. 2003 A new laser vorticity probe – LAVOR: its development and validation in a turbulent boundary layer. *Exps. Fluids* **34**, 192–205.

ANDREOPOULOS, J. 1983*a* Improvements of the performance of triple hot wire probes. *Rev. Sci. Instrum.* **54**, 733–740.

ANDREOPOULOS, J. 1983*b* Statistical errors associated with turbulence intensity and probe geometry in hot-wire anemometry. *J. Phys.* E. *Sci. Instrum.* **16**, 1264–1271.

ANDREOPOULOS, J. & AGUI, J. 1996 Vorticity flux dynamics in a two-dimensional turbulent boundary layer. *J. Fluid Mech.* **309**, 45–84.

ANDREOPOULOS, Y., AGUI, J. H. & BRIASSULIS, G. 2000 Shock wave turbulence interactions. *Ann. Rev. Fluid Mech.* **32**, 309–345.

ANDREOPOULOS, Y. & HONKAN, A. 1996 Experimental techniques for highly resolved measurements of rotation, strain and dissipation-rate tensors in turbulent flows. *Meas. Technol.* **7**, 1462–1472.

ANDREOPOULOS, Y. & HONKAN, A. 2001 An experimental study of the dissipative and vortical motions in turbulent boundary layers. *J. Fluid Mech.* **439**, 131–163.

ANDREOPOULOS, J. & MUCK, K. C. 1987 Some new aspects of the shock-wave boundary layer interaction in compression ramp corner. *J. Fluid Mech.* **180**, 405–428.

ANYIWO, J. C. & BUSHNELL, D. M. 1982 Turbulence amplification in shock-wave boundary layer interaction. *AIAA J.* **20**, 893–899.

BARRE, S., ALLEM, D. & BONNET, J. P. 1996 Experimental study of normal shock/homogeneous turbulence interaction. *AIAA J.* **34**, 968–974.

BARRE, S., BONNET, J. P., GATSKI, T. B. & SANDHAM, N. D. 2000 Compressible high speed flows. In *Closure Strategies for Modeling Turbulent and Transitional Flows* (ed. B. E. Launder & N. D. Sandham). Cambridge University Press.

BATCHELOR, G. K. & TOWNSEND, A. A. 1947 Decay of vorticity in isotropic turbulence. *Proc. R. Soc. Lond.* A **199**, 238–255.

BENDAT, J. S. & PIERSOL, A. G. 2000 *Random Data Analysis and Measurements Procedures*. Wiley.

BRIASSULIS, G. K. 1996 Unsteady nonlinear interactions of turbulence with shock waves. PhD Thesis, City College of City University of New York.

BRIASSULIS, G., AGUI, J. & ANDREOPOULOS, Y. 2001 The structure of weakly compressible grid turbulence. *J. Fluid Mech.* **432**, 219–283 (referred to herein as BAA).

BRIASSULIS, G., AGUI, J., ANDREOPOULOS, J. & WATKINS, C. B. 1996 A shock tube research facility for high-resolution measurements of compressible turbulence. *Expl Therm. Fluid Sci.* **13**, 430–446.

BRIASSULIS, G. K. & ANDREOPOULOS, J. 1996. High resolution measurements of isotropic turbulence interacting with shock waves. *AIAA Paper* 96-0042.

BRIASSULIS, G., HONKAN, A., ANDREOPOULOS, J. & WATKINS, B. C. 1995 Applications of hot-wire Anemometry in Shock Tube Flows. *Exps. Fluids.* **19**, 29–37.

BUDZINSKI, J. M., ZUKOSKI, E. E. & MARBLE, F. E. 1992 Rayleigh scattering measurements of shock enhanced mixing. *AIAA. Paper* 92-3546.

CHU, B. T. & KOVASZNAY, L. S. G. 1957 Non-linear interactions in a viscous heat-conducting compressible flow. *J. Fluid Mech.* **3**, 494–514.

DEBIEVE, J. F. & LACHARME, J. P. 1985 *Shock Wave Free Turbulence Interactions, IUTAM Conference, Paris.*

DOSANJH, D. S. & WEEKS, T. M. 1964 Interaction of a starting vortex as well as Karman vortex streets with traveling shock wave. *AIAA Paper* 64–425.

DURBIN, P. A. & ZEMAN, O. 1992 Rapid distortion theory for homogeneous compressed turbulence with applications to modeling. *J. Fluid Mech.* **242**, 349–370.

HAAS, J. F. & STURTEVANT, B. 1987 Interaction of weak shock waves with cylindrical and spherical gas inhomogeneities. *J. Fluid Mech.* **181**, 41–58.

HANNAPPEL, R. & FRIEDRICH, R. 1995 Direct numerical simulation of a Mach 2 shock interacting with isotropic turbulence. *Appl. Sci. Res.* **54**, 205–221.

HESSELINK, L. & STURTEVANT, B. 1988 Propagation of weak shocks through a random medium. *J. Fluid Mech.* **196**, 513–553.

Honkan, A. & Andreopoulos, J. 1992 Rapid compression of grid-generated turbulence by a moving shock wave. *Phys. Fluids* A **4**, 2562–2572.

Honkan, A. & Andreopoulos, J. 1997 Vorticity strain-rate and dissipation characteristics in the near wall region of turbulent boundary layers. *J. Fluid Mech.* **350**, 29–96.

Honkan, A., Watkins, C. B. & Andreopoulos, J. 1994 Experimental study of interactions of shock wave with free stream turbulence. *Trans. ASME: J. Fluids Engng* **116**, 763.

Hunt, J. C. R. 1973 A theory of turbulent flow round two-dimensional bluff bodies. *J. Fluid Mech.* **61**, 625–636.

Hunt, J. C. R. & Carruthers, D. J. 1990 Rapid distortion theory and the problems of turbulence. *J. Fluid Mech.* **212**, 497–532.

Jacquin, L., Cambon, C. & Blin, E. 1993 Turbulence amplification by a shock wave and rapid distortion theory. *Phys. Fluids* A **5**, 2539–2550.

Jamme, S. 1998 Etude de l'interaction entre une turbulence homogène isotrope et une onde de choc. PhD Thesis, INS Toulouse, France

Keller, J. & Merzkirch, W. 1990 Interaction of a normal shock with a compressible turbulent flow. *Exps Fluids* **8**, 241–248.

Kerr, R. M. 1985 Higher-order derivative correlations and alignment of small structures in isotropic numerical turbulence. *J. Fluid Mech.* **153**, 31–54.

Lee, L., Lele, S. K. & Moin, P. 1993 Direct numerical simulation of isotropic turbulence interacting with a weak shock wave. *J. Fluid Mech.* **251**, 533–562.

Mahesh, K. A., Lele, S. K. & Moin, P. 1997 The influence of entropy fluctuations on the interaction of turbulence with a shock wave. *J. Fluid Mech.* **334**, 353–379.

McKenzie, J. F. & Westphal, K. O. 1968 Interaction of linear waves with oblique shock waves. *Phys. Fluids* **11**, 2350–2357.

Moffat, H. K. 1969 The degree of knottedness of tangled vortex lines. *J. Fluid Mech.* **35**, 137–145.

Mohamed, S. M. & LaRue, C. J. 1990 The decay power law in grid generated turbulence. *J. Fluid Mech.* **219**, 195–214.

Morkovin, M. V. 1960 Note on assessment of flow disturbances at a blunt body traveling at supersonic speeds owing to flow disturbances in free stream. *J. Appl. Mech.* **27**, 223–229.

Ribner, H. S. 1953 Convection of a pattern of vorticity through a shock wave. *NACA Rep.* 2864; also *NACA Rep.* 1164.

Ribner, H. S. 1986 Spectra of noise and amplified turbulence emanating from shock-turbulence interaction. *AIAA J.* **25**, 436–442.

Rotman, D. 1991 Shock wave effects on a turbulent flow. *Phys. Fluids* A **3**, 1792–1806.

Ruetsch, G. R. & Maxey, M. R. 1991 Small scale features of vorticity and passive scalar fields in homogeneous isotropic turbulence. *Phys. Fluids* A **3**, 1587–1593.

Sekundov, A. N. 1974 Supersonic flow turbulence and interaction with a shock wave. *Izv. Akad. Nauk SSR Mekh. Zhidk. Gaza*, March–April.

She, Z.-S., Jackson, E. & Orszag, S. A. 1991 Structure and dynamics of homogeneous turbulence. In *Turbulence and Stochastic Processes: Kolmogorov's Ideas 50 Years on* (ed. J. C. R. Hunt, O. M. Philips & D. Williams). The Royal Society, London.

Tennekes, H. & Lumley, J. L. 1972 *A First Course in Turbulence*. MIT Press.

Thomson, P. A. 1972 *Compressible Fluid Mechanics*. McGraw-Hill.

Tsinober, A., Kit, E. & Dracos, T. 1992 Experimental investigation of the field of velocity gradients in turbulent flows. *J. Fluid Mech.* **242**, 169–192.

Wallace, J. M., Balint, J. L. & Ong, L. 1992 An experimental study of helicity density in turbulent flows. *Phys. Fluids* A **4**, 2013–2026.

Xanthos, S., Briassulis, G. & Andreopoulos, Y. 2002 The interaction of decaying free stream turbulence with a moving shock wave: pressure field. *AIAA J. Propulsion Power* **18**, 1289–1297.

Zang, T. A., Hussaini, M. Y. & Bushnell, D. M. 1982 Numerical computations of turbulence amplification in shock wave interactions. *AIAA Paper* 82-0293.

Zwart, P., Budwig, R. & Tavoularis, S. 1997 Grid turbulence in compressible flow. *Exps. Fluids* **23**, 520–522.